University of Texas at Tyler

Scholar Works at UT Tyler

School of Medical and Biological Sciences
Faculty Publications and Presentations

School of Medical Biological Sciences

2-2022

SARS-CoV-2 Variants Increase Kinetic Stability of Open Spike Conformations as an Evolutionary Strategy

Ziwei Yang

Yang Han

Shilei Ding

Wei Shi

Tongqing Zhou

See next page for additional authors

Recommended Citation

Author

Ziwei Yang, Yang Han, Shilei Ding, Wei Shi, Tongqing Zhou, Andrés Finzi, Peter D. Kwong, Walther Mothes, and Maolin Lu

SARS-CoV-2 Variants Increase Kinetic Stability of Open Spike Conformations as an Evolutionary Strategy

Ziwei Yang,[a] Yang Han,[b] Shilei Ding,[c] Wei Shi,[d] [ID]Tongqing Zhou,[d] [ID]Andrés Finzi,[c] [ID]Peter D. Kwong,[d] [ID]Walther Mothes,[a] [ID]Maolin Lu[b]

[a]Department of Microbial Pathogenesis, Yale University School of Medicine, New Haven, Connecticut, USA
[b]Department of Cellular and Molecular Biology, University of Texas Health Science Center, Tyler, Texas, USA
[c]Centre de Recherche du CHUM (CRCHUM), Département de Microbiologie, Infectiologie et Immunologie, Université de Montréal, Montréal, Quebec, Canada
[d]Vaccine Research Center, National Institute of Allergy and Infectious Diseases, National Institutes of Health, Bethesda, Maryland, USA

Ziwei Yang and Yang Han contributed equally to this work. Author order was based on the starting dates of the co-first authors.

ABSTRACT Severe acute respiratory syndrome coronavirus 2 (SARS-CoV-2) variants of concern (VOCs) harbor mutations in the spike (S) glycoprotein that confer more efficient transmission and dampen the efficacy of COVID-19 vaccines and antibody therapies. S mediates virus entry and is the primary target for antibody responses, with structural studies of soluble S variants revealing an increased propensity toward conformations accessible to the human angiotensin-converting enzyme 2 (hACE2) receptor. However, real-time observations of conformational dynamics that govern the structural equilibriums of the S variants have been lacking. Here, we report single-molecule Förster resonance energy transfer (smFRET) studies of critical mutations observed in VOCs, including D614G and E484K, in the context of virus particles. Investigated variants predominantly occupied more open hACE2-accessible conformations, agreeing with previous structures of soluble trimers. Additionally, these S variants exhibited slower transitions in hACE2-accessible/bound states. Our finding of increased S kinetic stability in the open conformation provides a new perspective on SARS-CoV-2 adaptation to the human population.

IMPORTANCE SARS-CoV-2 surface S glycoprotein—the target of antibodies and vaccines—is responsible for binding to the cellular receptor hACE2. The interactions between S and hACE2 trigger structural rearrangements of S from closed to open conformations prerequisite for virus entry. Under the selection pressure imposed by adaptation to the human host and increasing vaccinations and convalescent patients, SARS-CoV-2 is evolving and has adopted numerous mutations on S variants. These promote virus spreading and immune evasion, partially by increasing the propensity of S to adopt receptor-binding competent open conformations. Here, we determined a time dimension, using smFRET to delineate the temporal prevalence of distinct structures of S in the context of virus particles. We present the first experimental evidence of decelerated transition dynamics from the open state, revealing increased stability of S open conformations to be part of the SARS-CoV-2 adaption strategies.

KEYWORDS SARS-CoV-2 variants, conformational dynamics, single-molecule FRET, spike glycoprotein, structure

Since the beginning of the severe acute respiratory syndrome coronavirus 2 (SARS-CoV-2) pandemic, variants of concern (VOCs) that are more transmissible and possibly more pathogenic have emerged and caused devastating consequences worldwide. The currently administered interventions, vaccines and antibody therapy, are directed
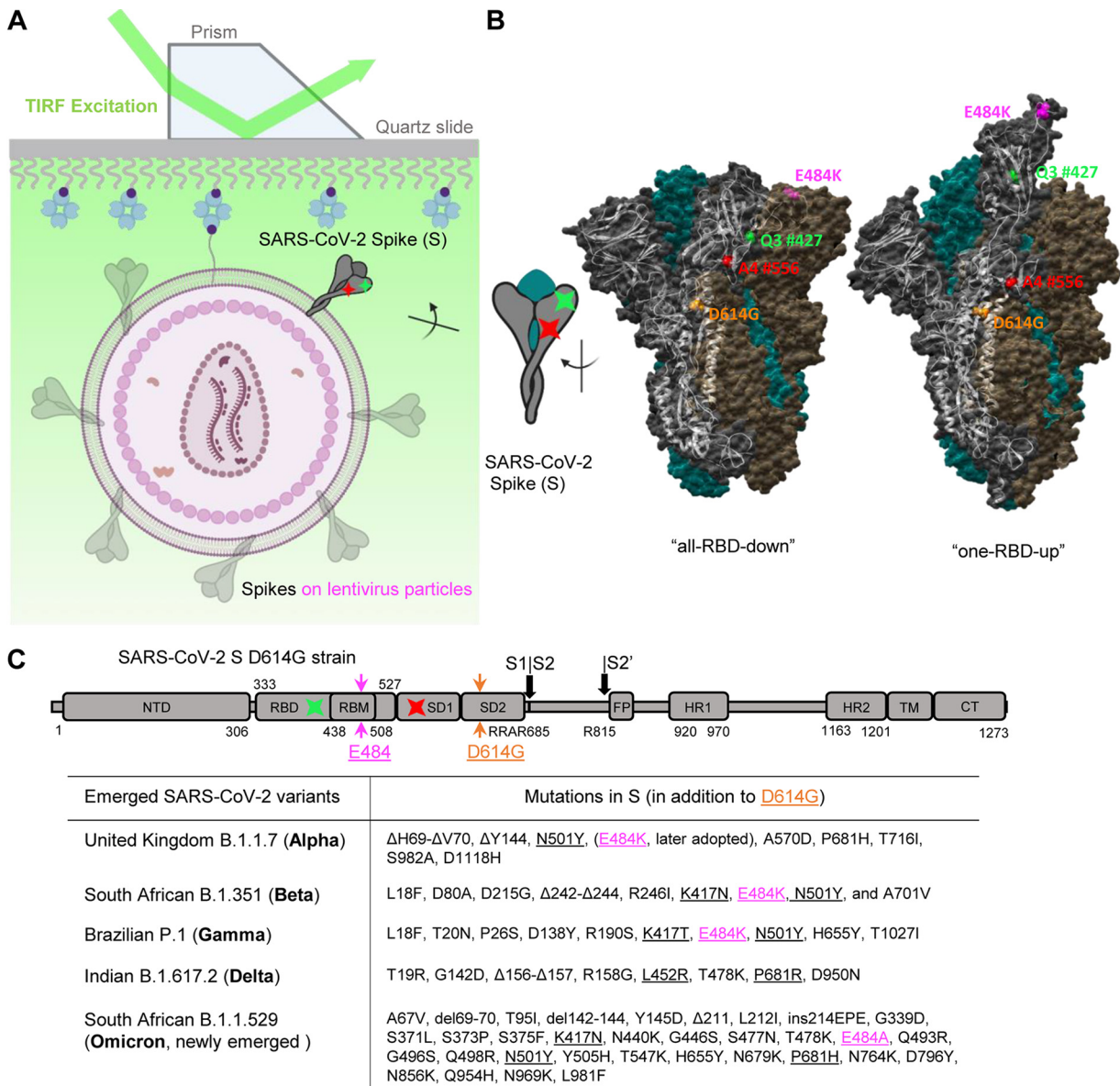
FIG 1 Experimental design for characterizing the conformational dynamics of the SARS-CoV-2 spike variants on virus particles via single-molecule FRET. (A and B) Experimental setup. (A) Virus-like particles that carry a single two-dye-labeled SARS-CoV-2 spike protomer among unlabeled wild-type spikes were immobilized on a quartz slide and then imaged on a prism-based total internal reflection fluorescence (TIRF) microscope. The quartz slide was passivated with PEG/PEG-biotin to enable streptavidin coating and the subsequent immobilization of virions that contain a biotin-lipid (DSPE-PEG-biotin). The virus-like particles were composed of HIV-1 cores and SARS-CoV-2 spikes on the virus surface. (B) Positioning of labeling dyes for the site-directed incorporation of fluorophores (LD555-cadaverine [a Cy3B derivative], green; LD655-CoA [a Cy5 derivative], red) was elucidated by the S1 conformational change from the RBD-down to the RBD-up structures, which are adapted from RCSB PDB codes 6ZB5 (all-RBD-down) and 7KJ5 (one-RBD-up). (C) Domain organization of the parental full-length SARS-CoV-2 spike protein with D614G and E484K mutations. The introduction sites of labeling tags Q3 (green) and A4 (red), where the donor and acceptor fluorophores will be conjugated to, respectively, are indicated. SD1, subunit domain 1; SD2, subunit domain 2; S1/S2, S2′, protease cleavage sites; FP, fusion peptide; HR1/HR2, heptad repeat 1/heptad repeat 2; TM, transmembrane domain; CT, cytoplasmic tail. Labeling peptides Q3 and A4 were inserted into RBD and SD1, respectively, before and after the RBM within the S protein in these studies. Emerged variants that are currently classified by CDC as variants of concern and their respective key mutations in the spike are specified in the table.

against the virus surface spike (S) protein as the primary target of antibody response (1–6). However, emerged and emerging SARS-CoV-2 variants harbor accumulated mutations in S (Fig. 1), including the D614G (S_{G614}), U.K. B.1.1.7 (S_{Alpha}), South African B.1.351 (S_{Beta}), Brazilian P.1 (S_{Gamma}), Indian B.1.617.2 (S_{Delta}), and the newly emerged B.1.1.529 ($S_{Omicron}$), of which some have gained increased resistance to antibody neutralization (7–19). While current vaccines remain efficient against severe disease

induced by these VOCs (20, 21), additional mutation in S could compromise this protection. Similarly, some VOCs are now resistant to first-generation antibody therapies and have impacted several molecular tests (11, 12, 17–19, 22–24). For instance, D614G is a spike variant that first emerged in January 2020 and became a dominant form as the pandemic spread, reaching >74% global prevalence by June 2020. D614G has been associated with increased infectivity and transmissibility of SARS-CoV-2 (25, 26). E484K has been identified as an escape mutation that facilitates virus immune evasion (27). E484K was first identified in South Africa (B.1.351) and Brazil (P.1), but it has also been gradually adopted by the U.K. (B.1.1.7) strain since, indicating an associated selective advantage (26). Other mutations on S variants such as L452R, N501Y, and P681R also attracted research attention due to enhanced angiotensin-converting enzyme 2 (ACE2) interaction and partial escape from vaccine-elicited antibodies (28). Therefore, it is of great importance that we understand how these mutations affect the conformational landscape of S and how this connects to the enhanced immune evasion, infectivity, and transmissibility of SARS-CoV-2 variants.

The S protein is a trimer of S1/S2 heterodimers (29, 30). The surface-exposing S1 contains the receptor-binding domain (RBD) that engages with cellular receptor human angiotensin-converting enzyme 2 (hACE2) (31–34), an event which, upon occurrence, triggers the transmembrane S2 to mediate the virus-cell membrane fusion process that enables virus entry (33–37). The S glycoprotein is structurally flexible and conformationally dynamic to facilitate both virus entry and antibody evasion. Each spike protomer samples two well-characterized RBD orientation-based conformations, the hACE2-accessible "RBD-up" and the hACE2-inaccessible "RBD-down" conformations (Fig. 1). Consequently, the S trimer can exist in an equilibrium of four possible combinations of the protomers, i.e., four conformational states of S trimer: "one-RBD-up," "two-RBD-up," "all-RBD-up," and "all-RBD-down." Extensive structural studies of truncated soluble and virus-associated parental/original S_{D614} strain have confirmed the existence of the above-mentioned major S trimer configurations (32–34, 38–46). As S continuously evolves, accelerated efforts have been implemented to characterize emerging S variants genetically, virologically, and structurally (28, 47–57). However, real-time monitoring of structural/conformational dynamics of S variants that connect structures has been lacking. The mechanism by which spike proteins adapt their conformations and dynamics during virus evolution could facilitate the understanding of pathogenesis, antibody neutralization, and vaccine efficacy of these S variants.

By using single-molecule Förster resonance energy transfer (smFRET), we have experimentally revealed that virus-associated S_{D614} dynamically samples at least four distinct conformational states, transitioning in time from milliseconds to seconds (58). On the faster dynamic scale, a remarkably long (~130 μs) sampling simulation of the S_{D614} opening process suggested the existence of five conformations between the transition from RBD-down to RBD-up (59), despite the temporal limitation that existed in simulation. Nevertheless, real-time experimental observations of conformational landscapes and the dynamics that govern the conformational equilibriums of recently emerged S variants on the viruses have not been performed. It is unclear whether arising S variants differ from the original S_{D614} on viruses regarding conformational dynamics/kinetics. In this study, we further deployed our smFRET approach to reveal the dynamic details and the mechanism of the conformational shifts in different S variants at the surface of lentivirus particles. Spike variants that contain our mutations of interest, D614G or/and E484K, as well as their parental strains were analyzed and compared side by side in this study. Using smFRET, we investigated how these mutations affect the conformational landscape and dynamics of the S glycoprotein by characterizing the overall movements within S in the millisecond to the second range. We discuss how such influences contribute to the selective advantage that variants harboring these mutations confer and provide insights into the mechanisms by which mutations in S could increase the severity of SARS-CoV-2 variants.

RESULTS

Establishing real-time monitoring of conformational profile of SARS-CoV-2 S variants via smFRET. To perform smFRET investigations of spike (S) variants, lentivirus particles that carry only a single FRET-paired dye-labeled SARS-CoV-2 spike protomer among unlabeled wild-type spikes were imaged on a prism-based total internal reflection fluorescence (TIRF) microscope (Fig. 1). Lentivirus particles contain the HIV-1 core and the SARS-CoV-2 S glycoproteins on the virus surface. As previously described (58), Q3 and A4 peptide tags were inserted before and after the receptor-binding motif (RBM) of tested S variants at positions 427 and 556 (427-Q3/556-A4 [Fig. 1]) to allow the site-specific introduction of donor and acceptor dyes/fluorophores onto S1 (see Materials and Methods). We previously validated that Q3 and A4 introduced at the specified locations did not affect viral infectivity (58). Lentivirus particles used for smFRET imaging were prepared by transfecting 293T cells with a 20-fold excess of plasmid encoding S_{D614}, S_{G614}, S_{Alpha}, or $S_{Alpha+E484K}$ over their corresponding 427-Q3/556-A4 plasmid. Statistically, this strategy, similarly used for the analogous investigations of HIV-1 envelope (60, 61), ensures the production of virus particles that contain, on average, only a single Q3/A4-tagged FRET-engineered S protomer within a hybrid trimer (tagged-wildtype-wildtype) among elsewhere wild-type S trimers on the virus. Enzymes (62, 63) that site specifically recognize amino acids in respective Q3 and A4 tags transfer customized dye-conjugated substrates to these tags (58); in this way, the donor and acceptor dyes (LD555, green; LD655, red) were introduced into the S1 site of S variants (Fig. 1A). Fluorescently labeled lentivirus particles were then immobilized on a quartz slide and imaged on a prism-based TIRF microscope. Donor fluorophores were directly excited by a single-frequency (532 nm) continuous-wave laser, and fluorescence emissions from both donor and acceptor were separately recorded at 25 Hz (Fig. 2B and Fig. 3C and E; see also Fig. S1A and B in the supplemental material). Conformational motions in the spike will lead to changes in the interdye distance exampled by structural switching from RBD-down to RBD-up (Fig. 1B), causing the donor-to-acceptor energy transfer efficiency (FRET efficiency) changes. FRET values can be derived by fluorescence signals of FRET-paired dyes in real time. In smFRET experiments, we extracted fluorescence traces from the recorded movies that demonstrate anticorrelated levels of donor and acceptor fluorescence and derived FRET traces (Fig. 2B, Fig. 3C and 3E, and Fig. S1A and B) to reflect conformational changes in the spike structures.

D614G substitution induces a conformational shift of virus-associated spikes toward receptor-accessible states. We first tested S-dependent infectivity of lentivirus particles on hACE2-expressing 293T cells (293T-ACE2). Virus particles bearing S_{G614}, $S_{G614+N501Y}$, $S_{G614+E484K}$, $S_{G614+E484K+N501Y}$, S_{Alpha}, or E484K-carrying S_{Alpha} ($S_{Alpha+E484K}$) variants had a discernible increase in infectivity compared to viruses bearing the parental S_{D614} (Fig. 2A), in agreement with previous results (52, 53, 56, 64, 65).

To determine whether D614G substitution on S would influence the conformational profiles of spike proteins, we next performed smFRET analyses of S_{G614} on lentivirus particles compared to the original S_{D614}. The example fluorescence donor/acceptor trace and the derived FRET efficiency trace of an individual S_{G614} on the virus (Fig. 2B) show that S_{G614} primarily occupies the 0.3-FRET (dashed red line)-indicated conformation and constantly interconverts between four conformational sates indicated by four different FRET levels (01-FRET, 0.3-FRET, 0.5-FRET, and 0.75-FRET). We have previously shown that S_{D614} on both lentivirus-like and coronavirus-like particles exists in four distinct FRET states: the 0.5-FRET state is the mostly abundantly occupied, and it corresponds to the "all-RBD-down" closed conformation; the 0.3-FRET state corresponds to the "one/two-RBD-up" partially open fusion-promoting conformation; the 0.1-FRET state corresponds to the "all-RBD-up" fully open fusion-activated conformation; and the high-FRET (slightly varied values) is an unknown state (58). We confirmed our reported results of S_{D614} primarily being in the all-RBD-down conformation from a newly generated conformational population-indicated FRET histogram (Fig. 2C), compiled of hundreds of FRET traces. In contrast, the FRET histogram of unbound S_{G614} on
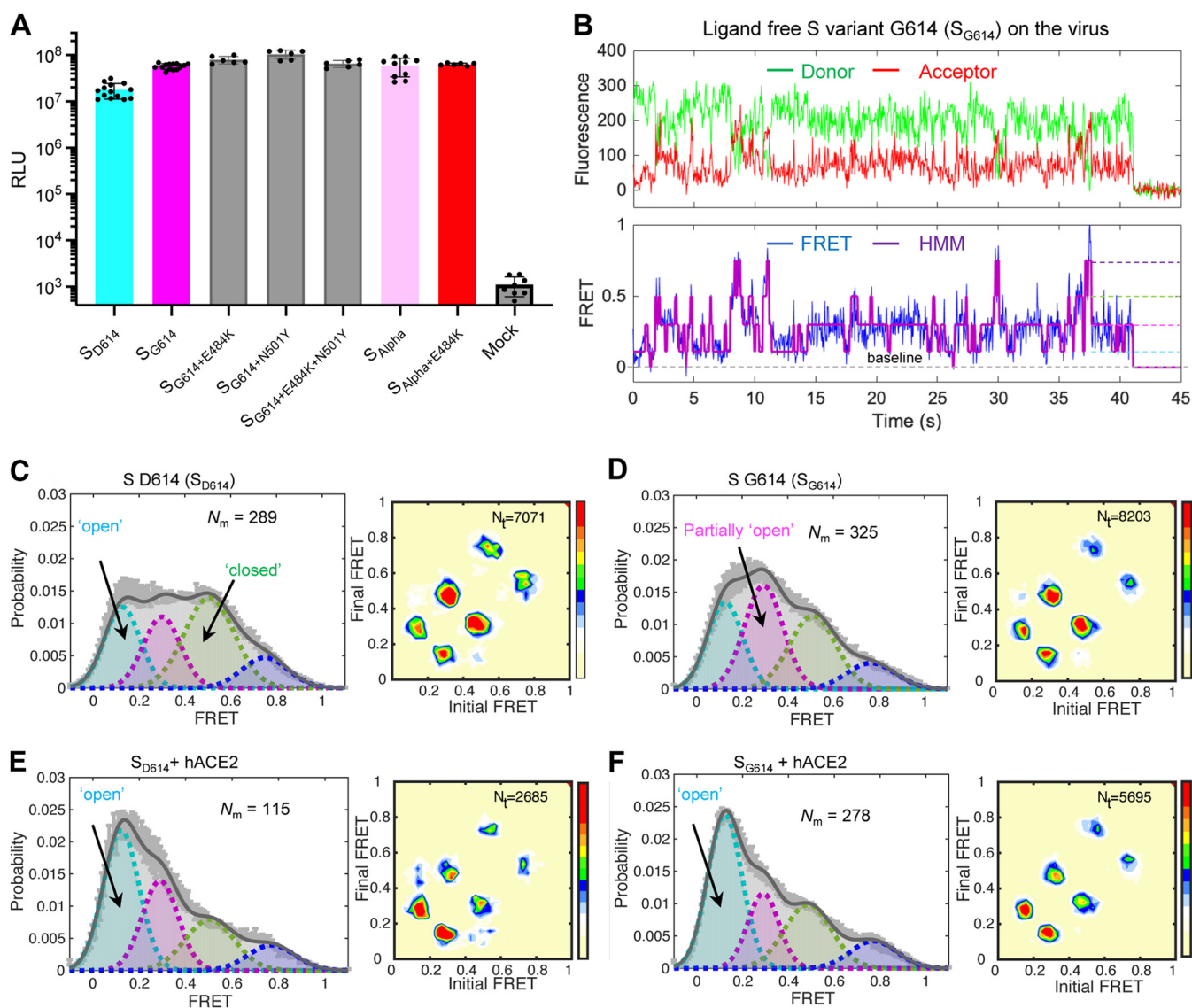
FIG 2 D614G substitution shifts the conformational landscape of unbound spike from the ground state to asymmetrically configured intermediate states. (A) Infectivity quantification for HIV-1 lentivirus particles carrying various spike variants determined on hACE2 expressing 293T cells (293T-ACE2). Infectivity (mean ± SD) was measured from three independent experiments in triplicates. RLU, relative light units. (B) Example fluorescence traces (LD555, green; LD655, red) and resulting quantified FRET traces (FRET efficiency, blue; hidden Markov model initialization, red) of a dually labeled ligand-free spike protein on the surface of HIV-1 lentivirus particle. The single-step photobleaching of dyes at the single-molecule level defined the baseline (dashed black). Four distinguishable FRET-populated states are indicated as color-coded dashed lines. (C and D) FRET histograms (left) and TDPs (right) of ligand-free D614 spike (S_{D614} [C]) and G614 spike (S_{G614} [D]) on lentivirus particles. A number (N_m) of individual active/dynamic molecule-FRET traces were compiled into a conformation-population FRET histogram (gray lines) and fitted into a 4-state Gaussian distribution (solid black) centered at 0.1-FRET (dashed cyan), 0.3-FRET (dashed red), 0.5-FRET (dashed green), and 0.75-FRET (dashed magenta). TDPs show the distributions of initial and final FRET values for every observed transition in FRET traces. TDPs are displayed as initial FRET versus final FRET with relative frequencies (max red scale = 0.01 transitions/second), originated from the idealization of individual FRET traces in FRET histograms. TDPs trace the locations of state-to-state transitions and their relative frequencies. (E and F) Experiments as in panels C and D, respectively, conducted in the presence of 200 µg/mL of monomeric hACE2. The soluble hACE2 activates spike proteins on the virus by shaping the conformational landscape toward stabilizing the all-RBD-up conformation (activated state). FRET histograms represent mean ± SEM, determined from three randomly assigned populations of FRET traces under corresponding experimental conditions. For evaluated relative state occupancies, see Table S1.

lentiviral particles demonstrate that S_{G614} inherits all four conformations from the S_{D614} with a shift in the conformational landscape (Fig. 2D). S_{G614} exhibits a propensity to occupy the 0.3-FRET indicated one/two-RBD-up partially open states, in which either one or two RBDs are exposed for hACE2 binding (Fig. 2D). Thus, D614G substitution shifts the conformational landscape of the original S_{D614} from hACE2-inaccessible all-RBD-down conformation dominance to predominately hACE2-accessible conformations. Our findings are consistent with the observations of increased occupancy of RBD-up structures characterized by cryo-electron microscopy (cryo-EM), despite the
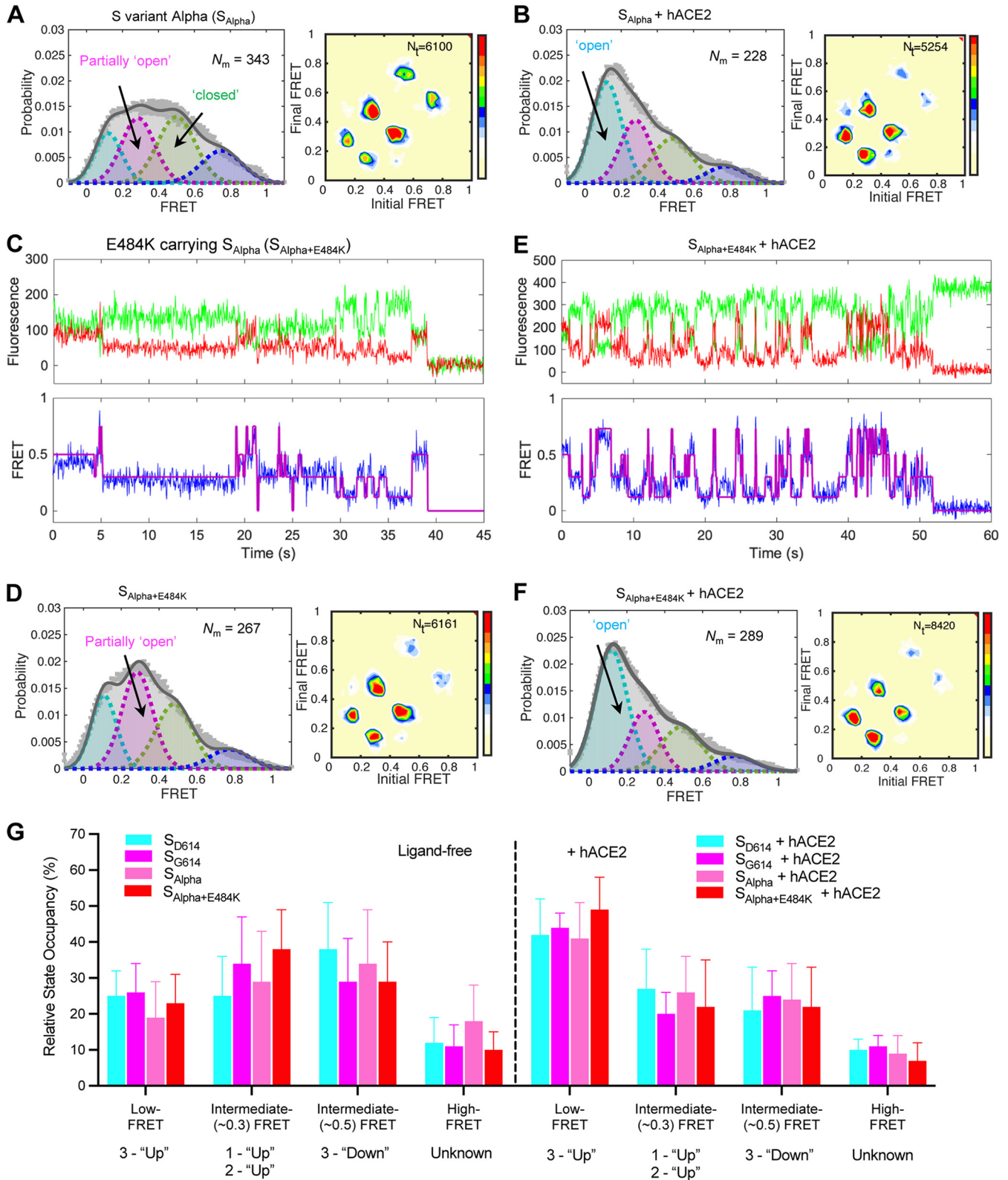
FIG 3 E484K stabilizes the S_{Alpha} variant toward RBD-up conformations. (A and B) FRET histograms (left) and TDPs (right) of S_{Alpha} variant on lentivirus particles with (A) and without (B) 200 μg/mL of hACE2. The soluble hACE2 activates S_{Alpha} by shaping the conformational landscape toward stabilizing the all-RBD-up conformation. (C) Representative fluorescence traces (LD555, green; LD655, red) and quantified FRET traces of a single ligand-free E484K-carrying S_{Alpha} variant ($S_{Alpha+E484K}$) on lentivirus particles. (D) FRET histogram (left) and TDP (right) of ligand-free $S_{Alpha+E484K}$ on lentivirus particles. (E and F) Experiments as in panels C and D, conducted in the presence of 200 μg/mL of hACE2. FRET histograms represent means ± SEM, determined from three randomly assigned populations of all FRET traces under corresponding experimental conditions. (G) Quantification of the FRET-indicated state occupancy for different spike variants. The occupancy in each FRET state was presented as mean ± SEM, determined by estimating the area under each Gaussian curve in FRET histograms. For fitting parameters, see Table S1.

variations in quantification among all published structural work (51–54, 64). In the presence of the hACE2, both S_{D614} and S_{G614} adopt the 0.1-FRET dominant patterns (Fig. 2E and F), meaning that higher proportion of spikes on the virus surface are in all-RBD-up fully open fusion-active conformations. The relative state occupancies were quantified (Table S1). The propensity toward the fully open conformation (0.1-FRET) can be directly observed from the individual FRET traces (Fig. S1).

Next, we sought to gain insights into the sequence and the frequency of conformational dynamics of S_{D614G}. We applied the hidden Markov model (HMM) (66) to idealize all FRET traces compiled into the FRET histogram individually and quantitatively analyzed thousands of transitions observed for the S glycoproteins on the viruses. The order and the frequency of transitions were displayed on transition density plots (TDPs) as distributions of initial FRET versus final FRET of all transitions (Fig. 2C to F, right graphs). The comparison of TDPs between S_{D614} and S_{G614} (Fig. 2C and D, right graphs) shows that conformational changes for S glycoproteins exhibited a defined sequence from the all-RBD-down closed state (0.5-FRET) to the all-RBD-up activated state (0.1-FRET) through a necessary intermediate 0.3-FRET state: one/two-RBD-up. This finding implies that the D614G substitution does not alter the sequence of events that constitute the conformational dynamics of the spike, although it does induce shifting of the conformational landscape/distribution (Fig. 2C and D). Similarly, the sequence of conformational transitions of hACE2-bound S_{D614} or S_{G614} remained identical to that for the ligand-free spike proteins (Fig. 2 and 3). The conformational distribution of the spike population, however, shifted toward an all-RBD-up-predominate state upon hACE2 binding (Fig. 2E and F).

E484K-carrying S_{Alpha} resides predominately in partially open one/two-RBD-up receptor-accessible conformations. E484K and N501Y reside in the RBM of spike that directly contacts the receptor hACE2 (Fig. 1B). All three S variants, S_{Alpha} (later strain), S_{Beta}, and S_{Gamma}, share both N501Y and E484K substitutions (Fig. 1C); E484K was later adopted by the Alpha variant after the emergence of the Beta and Gamma variants. Increasing experimental evidence indicates that E484K enables immune evasion, while N501Y may foster increased virus transmissibility by enhancing hACE2 binding (7, 8, 27, 47, 67, 68). Analysis of the FRET histogram and TDP of ligand-free S_{Alpha} on lentivirus particles revealed that S_{Alpha} (Fig. 3A) sampled slightly more one/two-RBD-up (partially open conformations) on the viruses than S_{D614} but less than S_{G614} (Fig. 2C and D and Table S1). This finding partially contradicts the cryo-EM structural results (55, 56), which indicate soluble forms of S_{Alpha} being more open than the same engineered soluble forms of S_{D614} and S_{G614}. Structural results lack the consideration of the activated state: a fully open three-RBD-up conformation. smFRET revealed *in situ* conformations of S_{Alpha} incorporated on virus particles, whereas cryo-EM characterized the soluble forms of S_{Alpha} protein. The differences in techniques likely contributed to the variations in the characterizations of the conformation occupancy. Encouragingly, parallel *in situ* characterizations of two antibody-bound S_{Alpha} proteins by smFRET and cryo-electron tomography (cryo-ET) resulted in an overall agreement in the number of individual RBD units with different conformations (57), despite the fact that smFRET is a dynamics-emphasizing approach, whereas cryo-ET and other structural tools emphasize static features. Overall, the hACE2 binding resulted in shifting of the S_{Alpha} conformational landscape toward a more fusion-active all-RBD-up-dominating state as expected (Fig. 3B).

To further assess the conformational effects of E484K in the context of S_{Beta}, S_{Gamma}, and S_{Alpha} (S_{Alpha} later adopted E484K), we next performed smFRET studies using E484K-carrying $S_{Alpha+484K}$ (Fig. 3C to F). E484K substitution exhibited a noticeable effect of reducing the occupancy of ligand-free spike variant in the 0.5-FRET state and increasing the 0.3-FRET state occupancy (Fig. 3C and D). This suggests that E484K stabilizes the S variants toward the one/two-RBD-up conformation by reducing the all-RBD-down conformation. The overall conformational landscape of ligand-free $S_{Alpha+E484K}$ (Fig. 3D) is similar to that of S_{G614} (Fig. 2D), with slightly elevated occupancy in the one/two-RBD-Up conformations. The observation that E484K renders

S variants adopting more one/two-RBD-up conformations agrees with all existing high-resolution cryo-EM structural results of E484K carrying S_{Beta} and S_{Gamma} (55, 56). The similarity between overall conformational distributions (FRET histograms) of $S_{Alpha+E484K}$ and S_{G614} is also in line with the structural and biochemical observations that highlighted the consistency between the structural and biochemical profiles of the E484K-containing S_{Beta} and S_{G614} variants (56). Interestingly, structural characterization of hACE2-bound S variants has been rarely reported. In our study, smFRET investigations of ligand-free and hACE2-bound S variants were done in parallel in a lentivirus context. Analysis of hACE2-bound $S_{Alpha+E484K}$ (Fig. 3E and F) and other variants in this study demonstrates that the parental spike and variants are unambiguously predominated by the all-RBD-up (0.1-FRET) activated state upon binding to hACE2 receptors (Fig. 3G). Figure 3E shows an example of a single spike molecule undergoing fast transition between the closed and open states, thus facilitating binding of hACE2. The quantifications of relative conformation occupancy for all inspected S variants are summarized in Fig. 3G, and the determining parameters are listed in Table S1.

Spike variants show a propensity toward RBD-up conformations with decelerated transition dynamics compared with that of RBD-down conformations. Our conformational results of all inspected S variants and their hACE2-bound states were further supported by the contour plots (maps), which display the FRET values across the entire 15-s duration of FRET detection (including those photobleached, zero-FRET values) in an unbiased fashion (Fig. 4A). Contour plots demonstrate an increased number of the S_{G614} variant occupying partially open one/two-RBD-up intermediates (0.3-FRET range) compared to the original S_{D614}, whose spikes are more enriched in the all-RBD-down (0.5-FRET range). Similarly, the E484K-containing S_{Alpha} variant also exhibits a higher frequency of spikes occupying the one/two-RBD-up intermediates (0.3-FRET) state than wild-type S_{Alpha}. Upon hACE2 binding, all the inspected variants exhibit an increase in spike density toward the low FRET range. This indicates that a shift of the spike conformational landscape from an all-RBD-down closed conformation or one/two-RBD-up partially open conformation to an all-RBD-up fully open fusion-activated conformation has taken place. This ensembled representation of spike conformational landscape corroborates the conclusion deduced from the histogram built upon visually identified noise-avoiding traces and suggests that our real-time observation of conformation population is robust despite the limited capacity of identifying potentially transiently (below milliseconds) sampled states.

One of the unique features of smFRET analysis is experimental evaluation of the transitioning kinetics among conformations of S variants in the context of virus particles by determining the transition rate between spike conformations (Fig. 4B). The dwell times of each FRET-defined conformation describe the duration of time that each spike stays within a specific conformation before changing into the next. They were first identified by applying hidden Markov modeling (HMM) and were then compiled into dwell time distributions. Dwell time distributions are displayed in survival probability plots (Fig. S2 and S3) as the probability function of durations of spike occupying a particular conformation in a directional transition event. Two-component exponential decays were the simplest model to interpret our data. The weighted transition rate derived from the exponential fitting for each transition event signifies the speed at which the spike transitions from the current conformation to the next. The final rate constants for all transition events are listed in a heat map (Fig. 4B), in which the smaller numbers are colored in red and larger numbers in green. The heat map of transition rates of different S variants amplifies subtle differences and reveals an exciting feature hidden in the interconverting map among four distinct conformations. We observed decreases in transition rates as the spikes progress through sequential changes from the all-RBD-down closed state to the all-RBD-up fully open activated state (Fig. 4B). This indicates that the spike trimer tends to dwell longer in hACE2-accessible one/two/all-RBD-up conformations. The finding of S_{G614} sampling more dynamics-reduced hACE2-accessible conformations implies its increased binding competence of

A

B

k

Transition rate decreases

"RBD-up" (open states) ← … → "RBD-down" (closed)
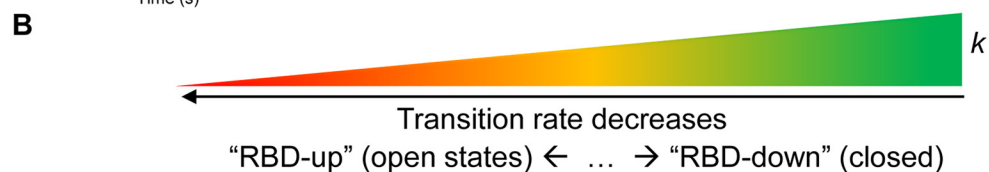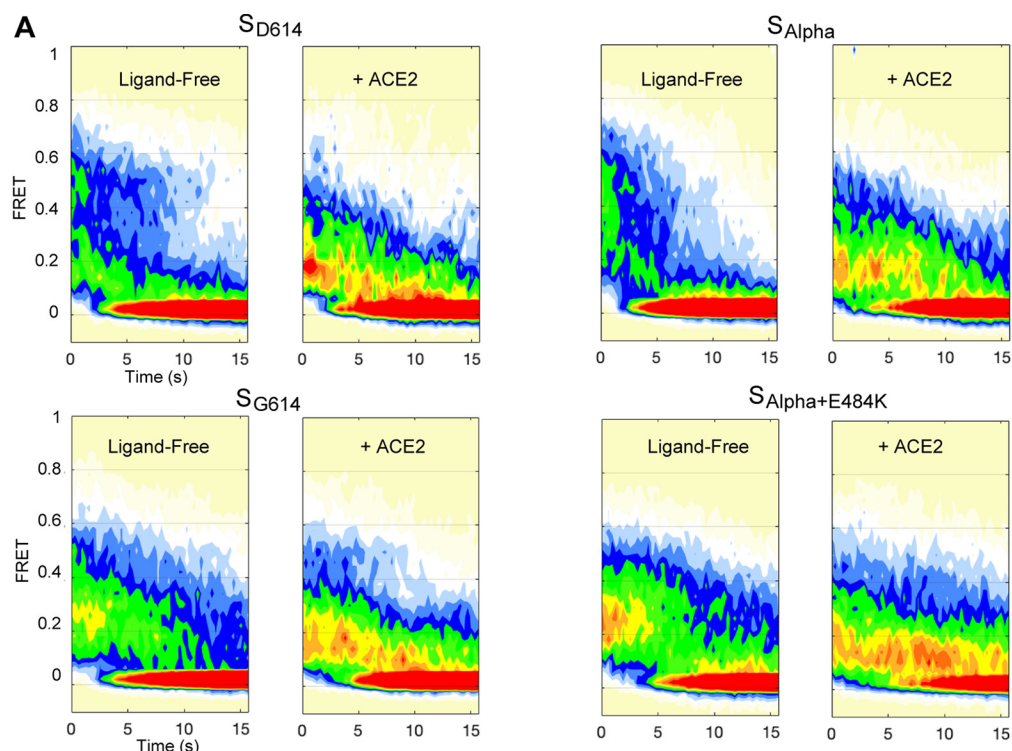
Spike variants on virus particles	$k_{0.11\rightarrow0.30}$ (s^{-1})	$k_{0.30\rightarrow0.11}$ (s^{-1})	$k_{0.30\rightarrow0.50}$ (s^{-1})	$k_{0.50\rightarrow0.30}$ (s^{-1})	$k_{0.50\rightarrow0.75}$ (s^{-1})	$k_{0.75\rightarrow0.50}$ (s^{-1})
S_{D614}						
Ligand-free	1.98 +/- 0.03	2.99 +/- 0.03	2.84 +/- 0.03	3.18 +/- 0.04	3.09 +/- 0.02	3.68 +/- 0.04
+hACE2	1.28 +/- 0.01	1.96 +/- 0.01	2.02 +/- 0.02	3.41 +/- 0.03	3.26 +/- 0.04	3.12 +/- 0.03
S_{G614}						
Ligand-free	1.55 +/- 0.02	2.13 +/- 0.02	1.97 +/- 0.02	2.73 +/- 0.02	3.29 +/- 0.03	3.74 +/- 0.03
+hACE2	1.17 +/- 0.01	1.92 +/- 0.03	1.96 +/- 0.02	2.64 +/- 0.03	2.97 +/- 0.02	3.22 +/- 0.03
S_{Alpha}						
Ligand-free	1.63 +/- 0.02	2.29 +/- 0.04	2.24 +/- 0.03	2.43 +/- 0.02	2.56 +/- 0.02	3.57 +/- 0.03
+hACE2	1.24 +/- 0.01	2.25 +/- 0.02	1.96 +/- 0.03	3.15 +/- 0.03	3.41 +/- 0.03	4.05 +/- 0.02
$S_{Alpha+E484K}$						
Ligand-free	1.6 +/- 0.01	1.92 +/- 0.02	1.84 +/- 0.02	2.81 +/- 0.02	3.1 +/- 0.03	3.59 +/- 0.04
+hACE2	1.37 +/- 0.01	1.99 +/- 0.02	1.81 +/- 0.02	2.33 +/- 0.02	2.64 +/- 0.02	3.54 +/- 0.03

FIG 4 D614G and E484K substitutions render S on the virus in favor of RBD-up open conformations, which are slower in temporal transitions. (A) Contour plots constructed from the compilation of the population of smFRET traces/trajectories.

(Continued on next page)

spikes to hACE2 and enhanced kinetic stability compared to those of S_{D614}. This likely explains the inconsistency reported previously surrounding hACE2 binding affinity and structural flexibility or stability of the soluble S_{G614} (51–54, 64).

Our results of transition rates among four different conformations indicate that the spike protomer is more conformationally stable in the RBD-up conformation than in the RBD-down. Thus, it is not surprising that hACE2-bound spikes (all-RBD-up) showed the least propensity to shuttle back to the upstream conformations on the fusion path (Fig. 4B). Similarly, the all-RBD-up, hACE2-bound conformation showed the lowest relative free energy in the derived quantitative model for hACE2 activation (Fig. 5) from smFRET results. The ligand-free S_{G614} and $S_{Alpha+E484K}$ spikes primarily occupy the one/two-RBD-up partially open state (0.3-FRET), which presents the lowest relative free energy among all four FRET-defined states. In contrast, all hACE2-bound spikes exhibit the lowest relative free energy at the 0.1-FRET state, the most populated all-RBD-up fully open fusion-activated state. Of note, our observation is solely on the S1 subunit, and our results cannot inform the downstream conformations after the fusion-active open conformation of S1 with three RBDs oriented up. Taken together, the results of smFRET analysis of S variants revealed that S in the RBD-up (hACE2-accessible) conformations/structures exhibit increased conformational stability with decelerated dynamics, providing a new perspective of molecular interpretations that S variants evolve to favor RBD-up conformations.

DISCUSSION

SARS-CoV-2 VOCs (Fig. 1C) pose significant challenge to public health worldwide. All five variants (Fig. 1C) feature an initially worldwide adopted D614G mutation compared to the original Wuhan strain, while three of them contain an E484K mutation (E484K was also later adopted by the Alpha variant according to the World Health Organization [https://www.who.int/en/activities/tracking-SARS-CoV-2-variants/]) and Omicron contains E484A. As these variants outcompeted the previous strains to become the globally dominant strain, it is of great importance that we understand how these mutations within the spike influence the behavior and functionality of the spike. In this study, we have used smFRET to uncovered various aspects of such influence, which furthered our understanding of SARS-CoV-2's survival strategy during the pandemic that started in 2019.

Discussion on tagging spike proteins. Our smFRET approach in this study relies on site specifically tagging S glycoproteins for fluorescent labeling. We have performed various validation experiments for the applied tagged S glycoproteins previously (57, 58) as well as in this study. Our results indicate that tags (short peptides) have no significant effect on the conformational dynamics of the S glycoprotein. Both tagged and untagged spike glycoproteins exhibit the same infectivity (58). The conformational landscape of the labeled spike responds to mutations and ligands in agreement with cryo-EM and cryo-ET studies. For instance, 2C (S383C and D985C) substitutions shift the conformational dynamics toward the three-RBD-down conformation, in complete agreement with the cryo-EM study (39, 58). We recently performed parallel smFRET and cryo-ET studies of the unliganded and antibody-bound spikes and found excellent agreement (57). The conformational preferences of various tested convalescent-phase

FIG 4 Legend (Continued)

The contour plots were summed over time (15 s) of active/dynamic molecules compiled in the corresponding FRET histograms (Fig. 2C to F and Fig. 3A, B, D, and F). Some FRET-labeled active molecules that have reached photobleaching within 15 s contribute to the 0-FRET population. Contour plots blindly/unbiasedly monitor conformational ensembles occupied by virus-associated spike proteins over time. (B) Rates of transition between all observed FRET states for all tested S variants and their respective ligand-activated states. Rates are color-coded: warm color indicates relatively faster in transition, whereas cold color means slower in transition. The distribution of dwell times (Fig. S2 and S3) in each FRET state, determined through HMM, were fitted to the sum of two exponential distributions, $y(t) = A1 \exp^{-k1t} + A2 \exp^{-k2t}$, where $y(t)$ is the probability and t is the dwell time. The weighted average of the two rate constants from each fit is presented. Error bars represent 95% confidence intervals propagated from the kinetics analysis.
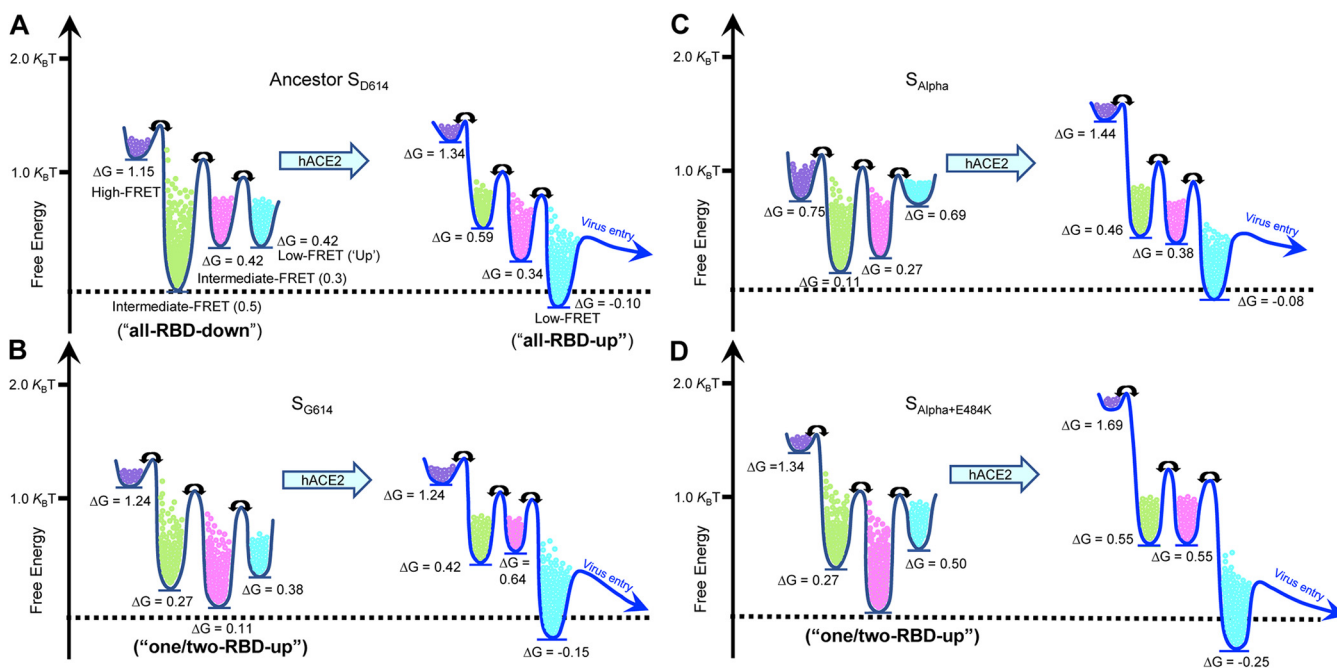
FIG 5 Relative free-energy models depict conformational landscapes of different virus-associated spike variants upon activation by the binding of hACE2. (A to D) Free-energy models of parental S_{D614} (A) and variants S_{G614} (B), S_{Alpha} (C), and $S_{Alpha+E484K}$ (D). The differences in free energies between states were roughly scaled based upon the relative state occupancies of each state. The ligand-free D614G- and E484K-carrying spikes are dominated by the intermediate-FRET state (one/two-RBD-up), which exhibits the lowest relative free energy among all four FRET states. In contrast, all hACE2-bound spikes show the lowest relative free energy at the low-FRET state (all-RBD-up).

patient sera and RBD-targeting and N-terminal-domain (NTD)-targeting antibodies for S are in agreement with antibody binding and virus neutralization studies in the Finzi, Ho, and other laboratories (58, 69). The response of the parental Wuhan strain and other tested variants to receptor ACE2 (this study) agrees with numerous structural and functional studies. The conformational landscape of D614G and E484K carrying S variants is consistent with various groups' structural studies (51–56, 64). Collectively, while we cannot exclude the possibility that there are slight changes in the conformational landscape of tagged compared to wild-type S glycoprotein, these observations indicate that the tags do not cause large conformational or functional changes to the spike.

The controversy of D614G on spike conformations and receptor binding: (i) enhancing conformational flexibility or stability and (ii) lower or higher binding affinity to hACE. D614G mutation in the S glycoprotein is associated with enhanced transmissibility of SARS-CoV-2 strains (70, 71). We showed that lentiviruses that contain D614G spike exhibit significant increase in infectivity compared to the original Wuhan strain. High-resolution cryo-EM structures of truncated soluble S_{G614} suggest that the naturally occurring S_{G614} is more conformationally flexible and favors the open conformations that are more accessible to hACE2, which likely accounts for enhanced virus transmissibility (52–54, 64). A recent cryo-EM work shows that full-length S_{G614} exhibits higher S trimer stability and lower binding affinity to hACE2 than the parental D614 (51), which contradicts several studies (52, 53, 71). The coexistence of enhanced transmissibility and reduced hACE2 binding was rationalized by attributing the transmissibility primarily to the effect of D614G substitution on preventing S1 from shedding off on the virion, which consequently increases the number of functional spikes on the viral surface (51). This explanation was supported by observing a disordered-to-ordered transition of a "630 loop" caused by the D614G substitution, which seemingly stabilizes S trimer in the one-RBD-up conformation, preventing premature S1 shedding (51). Our smFRET results are derived from fluorescent signals generated by FRET-paired dyes labeled on the spike variants on virus

particles tethered on the quartz slide. Fluorescence from shed spikes would diffuse and would not exhibit consistent spatial coordination (anticorrelation between donor and acceptor) in the movie and be excluded from the analysis. Thus, differences in shedding between variants do not affect our estimation of the conformation and dynamics of spike proteins. In contrast, our smFRET analysis revealed the conformational states and their interconverting dynamics of S1 in full-length S1/S2 trimer context embedded on the surface of viral particles.

By using smFRET, we determined that the S_{G614} variant exhibits a higher number of spikes residing in partially open conformations than S_{D614}, consistent with all available structural data (51–54). Spikes sampling more partially open one-RBD-up or two-RBD-up hACE2-accessible conformations could potentially favor more hACE2 binding toward the fully fusion-activated all-RBD-up conformation (52, 53). The observed lower transition rate of hACE2-accessible RBD-up conformations (Fig. 4B) can contribute to S trimer stability (51). Thus, our results of S_{G614} dwelling longer within more hACE2-accessible conformations likely reconcile the controversy of hACE2 binding and structural flexibility/stability of the soluble S_{G614} (51–54, 64, 71). The combined effect of D614G on enhancing S-hACE2 binding competence and stabilizing spikes in receptor-accessible conformations may confer the enhanced transmissibility of D614G-bearing SARS-CoV-2 VOCs.

Changing SARS-CoV-2 evolutionary adaptation: S-associated virus transmissibility versus immune evasion. The original S strain adopted a predominately all-RBD-down closed conformation, which helped conceal the RBD from host humoral responses (32, 34, 45, 58), potentially enabling the SARS-CoV-2 to better survive within the host. While S can only bind to hACE2 when the RBD is exposed, the concealment of the RBD may be an important immune evasion strategy for the virus, as RBD is a primary target of neutralizing antibodies. As a potential trade-off this protective trait, the receptor binding ability of S suffers due to the concealment of the RBD. However, subsequent variants carrying the D614G mutation within S have adopted another strategy. D614G reduces S1 shedding. This may in part reflect the finding that several RBD-targeting antibodies have been observed to shed S1 (57, 72, 73) and that evasion from these quite common antibodies may be accomplished by stabilization of spikes. Moreover, D614G also exhibits more functional spikes on the surface predominately in the hACE2-accessible conformations, which significantly increases the hACE2 binding competence and may contribute to an enhanced transmission rate. These results suggest that higher receptor binding competence and higher transmission rate may confer a higher fitness advantage for the spread of SARS-CoV-2 than a higher degree of protection against host immunity. Therefore, early SARS-CoV-2 evolution to the human host from late 2019 to early 2020 likely prioritized receptor binding competence to enhance transmissibility instead of the defense against host immunity.

In addition to D614G, E484K is another mutation adopted by most of the dominating strains, appearing in 3 of the 5 VOCs (Alpha, Beta and Gamma, despite E484A in Omicron), of which the Alpha variant later was similarly observed to adopt E484K according to the World Health Organization. The appearance of both E484K and N501Y mutations appears to increase the hACE2-binding affinity of S (56, 65). This characteristic trait indicates that E484K coexisting with N501Y also serves to increase the transmissibility of SARS-CoV-2. Our results suggest that like D614G, E484K achieves this by promoting the S conformation to shift from predominately all-RBD-down hACE2-inaccessible closed state to one/two-RBD-up hACE2-accessible partially open states, thus exposing the RBD and facilitating receptor binding of S. Similar to the case with D614G, emerged E484K-carrying S variants likely promote transmissibility by adopting more dynamics-decelerated or implied stability-enhanced fusion-promoting hACE2-accessible conformations, revealed by our smFRET results. Notably, E484K was also identified as an escape mutation, as it enables the virus to escape host antibody recognition (9, 27, 74–76). This immune-evasive trait could be caused by the reversal of electric charge at position 484 due to the E-to-K mutation, which creates a

disadvantaged electrostatic interaction site that likely weakens the binding efficiency of anti-RBD antibodies. The shift of electric charge could potentially cause local conformational changes in the RBD (16), which exceeds the capacity of our current smFRET setup. It is possible that this unique gain-of-function mutation was selected to reconcile the cost of exposing the RBD, which is a primary target of highly potent neutralizing antibodies. It could explain why the original Alpha variant, identified in the United Kingdom, did not contain the E484K mutation but has since adopted it. We also suspect that a reversal of electric charge (E to K) at the 484 location might have disrupted the local electrostatic interaction within the spike structure, which might have served as a latch that maintained the closed conformation, causing S to become more open. Structural studies have implied E484K as a local destabilizing factor in the structure that disrupts the native conformation of the RBD tip, hindering the binding of some RBD-directed neutralizing antibodies (55). The destabilization might loosen RBDs up and cause the reequilibrium of S conformations to favor RBD-up ones. By the time this study was performed, SARS-CoV-2 modified its survival strategy by adopting E484K in addition to D614G to confer higher transmissibility (likely complemented with N501Y) and protect S against antibodies. SARS-CoV-2 continues to evolve, and Omicron currently outcompetes Delta and other variants as the dominant pandemic form. SARS-CoV-2 could have shifted its survival strategy again, which requires further investigation of both Delta and Omicron.

In conclusion, we used smFRET to reveal real-time conformational populations adopted by virus-associated S variants and experimentally identified conformation-interconverting temporal dynamics. We found that S evolves to favor the hACE2-binding competent RBD-up conformations, and RBD-up conformations exhibit decelerated dynamics compared with RBD-down. Our results explain the inconsistent results regarding the hACE2 binding ability of S variants and S stability. Our findings improve the molecular understanding of earlier S variants underlying immune evasion and virus transmissibility and further provide the molecular basis of our knowledge and prediction on SARS-CoV-2 evolution, informing S-centric interventions to curtail the COVID-19 pandemic.

MATERIALS AND METHODS

Cell lines. 293T (or HEK293T) cells, 293T-ACE2, and Expi293F cells were cultured in Dulbecco modified Eagle medium (DMEM) supplemented with 10% fetal bovine serum (FBS), 100 U/mL penicillin/streptomycin, and 2 mM L-glutamine and in the presence of 5% CO_2. Cell culture medium was exchanged with fresh medium before transfection. 293 cells, human embryonic kidney cells, were obtained from the ATCC (catalog number CRL-1573). 293T cells were 293-derived cells with the simian virus 40 T antigen inserted. 293T-ACE2 cells, derived from 293T cells, stably express human ACE2 (77). Expi293F cells, derived from the 293 cells, were purchased from Thermo Fisher Scientific (catalog number A14528).

Construction of full-length untagged and tagged SARS-CoV-2 S variants. Our current FRET-engineered system uses enzymatic labeling that introduces peptide tags located sterically further from any of accumulated mutations on spike (S) variants. Untagged and double-tagged SARS-CoV-2 spike variants were generated based on a template full-length pCMV3-SARS-CoV-2 spike (codon optimized; Sino Biological; catalog number VG40589-UT) plasmid that has translated amino acid sequence identical to that of SARS-CoV-2 surface glycoprotein (GenBank accession no. QHD43416.1). As described previously (58), peptide-based labeling tags Q3 (GQQQLG) and A4 (DSLDMLEM) (62, 63) were engineered into the parental S D614 (S_{D614}, first identified in Wuhan) and tested variants at positions before and after the receptor-binding motif (RBM) to avoid interfering with the binding of cellular receptor human ACE2 (hACE2) (Fig. 1C). Insertion of a pair of 427-Q3/556-A4 tags into S did not compromise S-dependent lentivirus infectivity, and this double-tagged FRET-engineered S_{D614} (designated S_{D614} Q3/A4) was constructed for smFRET imaging of S_{D614} (58). D614G point mutation was introduced into both untagged full-length pCMV3 S_{D614} and double-tagged S_{D614} Q3/A4 constructs to generate both untagged and tagged S_{G614} variants. E484K and N501Y were further introduced into the untagged S_{G614} individually and together. In the case of the S_{Alpha} (pcDNA3.1 S_{Alpha}, codon-optimized) variant, DNA sequences encoding untagged or double-tagged (with tags positioning at the exact positions as in tagged S_{D614} or S_{G614}) were synthesized by GenScript and cloned into the pcDNA3.1 vectors. E484K point mutation was introduced into both untagged and tagged pcDNA3.1 S_{Alpha} by site-specific mutagenesis.

Viral infectivity measurements. The infectivity of lentivirus particles carrying S proteins (including variants) on the surface was evaluated using a vector containing an HIV-1 long terminal repeat (LTR) that expresses a *Gaussia* luciferase reporter (HIV-1-inGluc) (78, 79). 293T cells were transfected at 60 to 80% confluence with the plasmid encoding indicated full-length SARS-CoV-2 S glycoproteins, the

plasmid encoding an intron-regulated Gluc (HIV-1-inGluc), and a plasmid, pCMV delta R8.2, encoding HIV-1 Gag-Pol (Addgene; plasmid number 12263) using FuGENE 6 (Promega; number E2311). At 40 h posttransfection, lentivirus particles were harvested and filtered through a 0.45-μm filter (Pall Corporation), and virus titers were determined on target cells 293T-ACE2 that endogenously express hACE2. Lentivirus infectivity was determined 48 h postinfection by measuring *Gaussia* luciferase activity in the 293T-ACE2 supernatant using a Pierce *Gaussia* luciferase flash assay kit (Thermo Fisher Scientific; catalog number 16158).

hACE2 expression and purification. The hACE2 expression construct was synthesized (Gene Universal Inc., Newark, DE) and subcloned into corresponding pVRC8400 vectors. Monomeric (residues 1 to 615) human ACE2 proteins were produced as described previously (80). Briefly, DNA sequence encoding monomeric hACE2 followed by an HRV3C cleavage site, monomeric Fc tag, and 8×His tag at the 3′ end were synthesized and cloned into the pVRC8400 vector. The proteins were expressed by transiently transfecting Expi293F cells and then purified by protein A affinity columns. The Fc and 8×His tags were removed by overnight HRV3C digestion at 4°C. hACE2 proteins were further purified over a Superdex 200 16/60 column in pH 7.5 buffer solution containing 5 mM HEPES and 150 mM NaCl.

Preparation of lentivirus particles carrying S proteins for smFRET. Lentivirus particles carrying S proteins (the ancestor and variants) on the surface were prepared similarly to the method previously described for the parental S$_{D614}$ (58) and HIV-1 (60, 61, 81). Briefly, lentivirus particles were produced by pseudotyping an HIV-1 core with full-length S proteins. To conduct studies of S variants by smFRET, we introduced the labeling peptide tags Q3 and A4 at the same positions (427 and 556, respectively) in S1 of S$_{G614}$, S$_{Alpha}$, and E484K-carrying S$_{Alpha}$ (S$_{Alpha+E484K}$) variants as in previously reported S$_{D614}$ (58). Lentivirus particles used for smFRET imaging were made in 293T cells by transfecting a 20-fold excess of plasmid encoding S$_{D614}$, S$_{G614}$, S$_{Alpha}$, or S$_{Alpha+E484K}$ over their corresponding 427-Q3/556-A4 to ensure that, on average, every virus particle carried a single Q3/A4-tagged S protomer. Plasmids encoding indicated untagged wild-type S (or variants), the corresponding double-tagged/FRET-engineered S, and a lentivirus packaging delta R8.2 were used at a ratio of 20:1:21, respectively. 293T cells were transfected using FuGENE 6 with above-indicated plasmids to express spikes on the HIV-1 lentivirus particles. Particles were harvested 40 h posttransfection, filtered through a syringe filter with a 0.45-μm pore size, and sedimented through a 15% sucrose cushion at 25,000 rpm for 2 h. The virus pellets were then resuspended in pH 7.5 50 mM HEPES containing 10 mM MgCl$_2$ and 10 mM CaCl$_2$. Of note, the strategy of using an excess of plasmid-encoding wild-type S versus trace amounts of a plasmid expressing labeling-tag-carrying S ensures the production of virus particles that contain, on average, only a single FRET-engineered S protomer. While most virus particles carry untagged S, among the small portion of virus particles containing tagged S, more than 95% will carry one dually tagged protomer while the other two protomers remain wild type. The same strategy has been used in our previous smFRET studies (58, 60, 61, 81).

Fluorescent labeling of S proteins on lentivirus particles. Lentivirus particles were fluorescently labeled through site-specific labeling based on enzymatic reactions, as previously described (58, 60, 61, 81). Briefly, transglutaminase transferred a Cy3B(3S) derivative (LD555-cadaverine) from the cadaverine conjugate to the central glutamine residue (underlined) of the Q3 (GQQQLG) tag in S1. The AcpS enzyme catalyzed the attachment of the Cy5 derivative (LD655-coenzyme A [CoA]) to the serine residue of the A4 tag (DSLDMLEM). LD555-cadaverine (0.5 μM; Lumidyne Technologies), LD655-CoA (0.5 μM; Lumidyne Technologies), transglutaminase (0.65 μM; Sigma-Aldrich), and AcpS (5 μM, homemade) were added to the above-listed lentivirus particles prepared for smFRET and incubated at room temperature overnight. LD555-cadaverine and LD655-CoA were synthesized by the Scott Blanchard laboratory (Lumidyne Technologies) based on new-generation photostable Cy3/Cy5 organic dyes (82). DSPE-PEG2000-biotin (0.02 mg/mL; Avanti Polar Lipids) was then added to the reaction mixture and incubated for 30 min at room temperature with rotation. Labeled lentivirus particles were then purified to eliminate excess free dyes and lipids by ultracentrifugation for 1 h at 40,000 rpm over a 6% to 18% OptiPrep (Sigma-Aldrich) gradient. Purified fluorescently labeled lentivirus particles were stored at −80°C.

smFRET imaging data acquisition. All smFRET imaging experiments were performed on a home-built prism-based total internal reflection fluorescence (TIRF) microscope. Lentivirus particles carrying fluorescently labeled spike proteins were immobilized on polyethylene glycol (PEG)-passivated quartz slides coated with streptavidin. The evanescent field was generated at the interface between the quartz slide and the virus-containing sample solution by prism-based total internal reflection, with 532-nm continuous wave laser excitation (Laser Quantum). The donor fluorophore (LD555) labeled on the virus is excited by the generated evanescent field and can transfer energy at its excited states to the neighboring acceptor fluorophore (LD655). Fluorescence from both fluorophores was collected through a 1.27-numerical-aperture (NA) 60× water immersion objective (Nikon) and then optically separated by a 650 DCXR dichroic filter (Chroma) mounted on a MultiCam LS image splitter (Cairn Research). Fluorescence of donor (ET590/50; Chroma) and acceptor (ET690/50; Chroma) was separately and simultaneously recorded on two synchronized ORCA-Flash4.0 V3 scientific complementary metal oxide semiconductor (sCMOS) cameras (Hamamatsu) at 25 Hz for 80 s. Fluorescently labeled virus samples were imaged in pH 7.4 50 mM Tris buffer containing 50 mM NaCl, a cocktail of triplet-state quenchers, and an oxygen scavenger system (83). Where indicated, the conformational effects of hACE2 on S proteins were determined by preincubating fluorescently labeled viruses with 200 μg/mL of hACE2 for 90 min at room temperature before imaging, and smFRET imaging data were taken in the continued presence of 200 μg/mL of hACE2.

smFRET quantification and statistical analysis. The analysis of smFRET data was performed using a MATLAB-based customized SPARTAN software package (84). Both donor and acceptor fluorescence intensity of each labeled virus were recorded over 80 s. The background signals at the single-molecule level were first identified based on the single-step fluorophore bleaching point and subtracted from the recorded signals. For each recorded virus, donor and acceptor fluorescence intensity traces (fluorescence time trajectory) were then extracted and corrected for the donor-to-acceptor cross talk. The energy transfer efficiency from the donor to the acceptor (FRET values, simplified as FRET in graphs) was calculated over time according to the equation FRET = $I_A/(\gamma I_D + I_A)$, where I_D and I_A are the fluorescence intensities of donor and acceptor, respectively, and γ is the coefficient correcting for the difference in detection efficiencies of the donor and acceptor. We corrected the difference in donor and acceptor detection efficiencies as cameras and optics in microscopes respond slightly differently to different wavelengths. The correction coefficient (γ) was determined after averaging, comparing, and compromising the background from multiple detection channels (donor and acceptor) and tested with different laser powers and validated across different samples. FRET traces (FRET values as a function of real time) monitor the relative donor-to-acceptor distance over time, which reflects conformational dynamics of the donor/acceptor-labeled spike on the lentivirus in real time. Virus particles that fall into any of the following categories were automatically excluded from our data analysis: (i) lacking either donor or acceptor or both fluorophores, (ii) containing multiple labeled protomers, and (iii) containing more than one labeled spike on a single virus. In addition, FRET traces from individual viruses that met our initial selection criteria and displayed sufficient signal-to-noise (S/N) ratios and anticorrelated fluctuations in donor and acceptor fluorescence were manually picked for data analysis. The anticorrelated feature directly defines FRET-indicated conformational states, which indicate fully active/dynamic spikes on virus particles. Thus, only one FRET-labeled protomer within one S trimer on one lentivirus particle (1 protomer/1 trimer/1 virus particle) showing clear anticorrelated features of donor and acceptor fluorescence and single fluorescence bleaching point passed our filters. FRET traces included in our analysis were then compiled into FRET histograms, which reflect conformational ensembles. Based on visual inspection of fluorescence and FRET traces that revealed direct observations of state-to-state (conformation-to-conformation) transitions, FRET histograms were fitted into the sum of four Gaussian distributions using the least-squares fitting algorithm in MATLAB. Each Gaussian distribution represents one FRET-defined conformational state of S proteins, and the area under each Gaussian curve estimates the relative probability of S occupying each conformation. The relative occupancy of each conformational state was used to evaluate the difference in relative free energies between states i and j, according to the equation $\Delta G°_{ij} = -k_B T ln(P_i/P_j)$, where P_i and P_j are the occupancy of ith and jth states, respectively, k_B is the Boltzmann constant, and T is the temperature in kelvin. FRET traces compiled in the FRET histogram under indicated experimental conditions were idealized using a segmental K-means algorithm (66) with a 4-state hidden Markov model, providing the simplest explanation of our data. The frequency and order of idealized state-to-state transitions were displayed in a transition density plot (TDP). Dwell times of S in each state were compiled into survival probability plots which were fitted to the sum of two exponential distributions [$y(t) = A_1 exp^{-k_1 t} + A_2 exp^{-k_2 t}$], where $y(t)$ is the probability and t is the dwell time. The transition rates were determined by averaging the two rate constants weighted by their amplitudes.

Statistical analysis. Quantitative graphs and statistics, as indicated in figure legends, were analyzed using MATLAB (MathWorks) and Prism version 9.0.0 (GraphPad).

SUPPLEMENTAL MATERIAL

Supplemental material is available online only.

FIG S1, TIF file, 1.1 MB.

FIG S2, TIF file, 2.5 MB.

FIG S3, TIF file, 2.5 MB.

TABLE S1, TIF file, 2.3 MB.

data. M.L., Z.Y., and Y.H. made figures, tables, and models. S.D., W.S., T.Z., A.F., and P.D.K. provided reagents, especially hACE2. M.L., Z.Y., and W.M. wrote the manuscript with input from A.F. and P.D.K.

We declare no competing interests.

REFERENCES

1. Baden LR, El Sahly HM, Essink B, Kotloff K, Frey S, Novak R, Diemert D, Spector SA, Rouphael N, Creech CB, McGettigan J, Kehtan S, Segall N, Solis J, Brosz A, Fierro C, Schwartz H, Neuzil K, Corey L, Gilbert P, Janes H, Follmann D, Marovich M, Mascola J, Polakowski L, Ledgerwood J, Graham BS, Bennett H, Pajon R, Knightly C, Leav B, Deng W, Zhou H, Han S, Ivarsson M, Miller J, Zaks T, COVE Study Group. 2021. Efficacy and safety of the mRNA-1273 SARS-CoV-2 vaccine. N Engl J Med 384:403–416. https://doi.org/10.1056/NEJMoa2035389.
2. Polack FP, Thomas SJ, Kitchin N, Absalon J, Gurtman A, Lockhart S, Perez JL, Perez Marc G, Moreira ED, Zerbini C, Bailey R, Swanson KA, Roychoudhury S, Koury K, Li P, Kalina WV, Cooper D, Frenck RW, Jr, Hammitt LL, Tureci O, Nell H, Schaefer A, Unal S, Tresnan DB, Mather S, Dormitzer PR, Sahin U, Jansen KU, Gruber WC, C4591001 Clinical Trial Group. 2020. Safety and efficacy of the BNT162b2 mRNA Covid-19 vaccine. N Engl J Med 383:2603–2615. https://doi.org/10.1056/NEJMoa2034577.
3. Voysey M, Clemens SAC, Madhi SA, Weckx LY, Folegatti PM, Aley PK, Angus B, Baillie VL, Barnabas SL, Bhorat QE, Bibi S, Briner C, Cicconi P, Collins AM, Colin-Jones R, Cutland CL, Darton TC, Dheda K, Duncan CJA, Emary KRW, Ewer KJ, Fairlie L, Faust SN, Feng S, Ferreira DM, Finn A, Goodman AL, Green CM, Green CA, Heath PT, Hill C, Hill H, Hirsch I, Hodgson SHC, Izu A, Jackson S, Jenkin D, Joe CCD, Kerridge S, Koen A, Kwatra G, Lazarus R, Lawrie AM, Lelliott A, Libri V, Lillie PJ, Mallory R, Mendes AVA, Milan EP, Minassian AM, Oxford COVID Vaccine Trial Group, et al. 2021. Safety and efficacy of the ChAdOx1 nCoV-19 vaccine (AZD1222) against SARS-CoV-2: an interim analysis of four randomised controlled trials in Brazil, South Africa, and the UK. Lancet 397:99–111. https://doi.org/10.1016/S0140-6736(20)32661-1.
4. Sadoff J, Le Gars M, Shukarev G, Heerwegh D, Truyers C, de Groot AM, Stoop J, Tete S, Van Damme W, Leroux-Roels I, Berghmans PJ, Kimmel M, Van Damme P, de Hoon J, Smith W, Stephenson KE, De Rosa SC, Cohen KW, McElrath MJ, Cormier E, Scheper G, Barouch DH, Hendriks J, Struyf F, Douoguih M, Van Hoof J, Schuitemaker H. 2021. Interim results of a phase 1-2a trial of Ad26.COV2.S Covid-19 vaccine. N Engl J Med 384:1824–1835. https://doi.org/10.1056/NEJMoa2034201.
5. Marovich M, Mascola JR, Cohen MS. 2020. Monoclonal antibodies for prevention and treatment of COVID-19. JAMA 324:131–132. https://doi.org/10.1001/jama.2020.10245.
6. Lloyd EC, Gandhi TN, Petty LA. 2021. Monoclonal antibodies for COVID-19. JAMA 325:1015. https://doi.org/10.1001/jama.2021.1225.
7. Chen RE, Zhang X, Case JB, Winkler ES, Liu Y, VanBlargan LA, Liu J, Errico JM, Xie X, Suryadevara N, Gilchuk P, Zost SJ, Tahan S, Droit L, Turner JS, Kim W, Schmitz AJ, Thapa M, Wang D, Boon ACM, Presti RM, O'Halloran JA, Kim AHJ, Deepak P, Pinto D, Fremont DH, Crowe JE, Corti D, Virgin HW, Ellebedy AH, Shi P-Y, Diamond MS. 2021. Resistance of SARS-CoV-2 variants to neutralization by monoclonal and serum-derived polyclonal antibodies. Nat Med 27:717–726. https://doi.org/10.1038/s41591-021-01294-w.
8. Diamond M, Chen R, Xie X, Case J, Zhang X, VanBlargan L, Liu Y, Liu J, Errico J, Winkler E, Suryadevara N, Tahan S, Turner J, Kim W, Schmitz A, Thapa M, Wang D, Boon A, Pinto D, Presti R, O'Halloran J, Kim A, Deepak P, Fremont D, Corti D, Virgin H, Crowe J, Droit L, Ellebedy A, Shi PY, Gilchuk P. 10 February 2021. SARS-CoV-2 variants show resistance to neutralization by many monoclonal and serum-derived polyclonal antibodies. Res Sq https://doi.org/10.21203/rs.3.rs-228079/v1.
9. Wang P, Nair MS, Liu L, Iketani S, Luo Y, Guo Y, Wang M, Yu J, Zhang B, Kwong PD, Graham BS, Mascola JR, Chang JY, Yin MT, Sobieszczyk M, Kyratsous CA, Shapiro L, Sheng Z, Huang Y, Ho DD. 2021. Antibody resistance of SARS-CoV-2 variants B.1.351 and B.1.1.7. Nature 593:130–135. https://doi.org/10.1038/s41586-021-03398-2.
10. Wang Z, Schmidt F, Weisblum Y, Muecksch F, Barnes CO, Finkin S, Schaefer-Babajew D, Cipolla M, Gaebler C, Lieberman JA, Oliveira TY, Yang Z, Abernathy ME, Huey-Tubman KE, Hurley A, Turroja M, West KA, Gordon K, Millard KG, Ramos V, Da Silva J, Xu J, Colbert RA, Patel R, Dizon J, Unson-O'Brien C, Shimeliovich I, Gazumyan A, Caskey M, Bjorkman PJ, Casellas R, Hatziioannou T, Bieniasz PD, Nussenzweig MC. 2021. mRNA vaccine-elicited antibodies to SARS-CoV-2 and circulating variants. Nature 592:616–622. https://doi.org/10.1038/s41586-021-03324-6.
11. Liu Y, Liu J, Xia H, Zhang X, Fontes-Garfias CR, Swanson KA, Cai H, Sarkar R, Chen W, Cutler M, Cooper D, Weaver SC, Muik A, Sahin U, Jansen KU, Xie X, Dormitzer PR, Shi PY. 2021. Neutralizing activity of BNT162b2-elicited serum. N Engl J Med 384:1466–1468. https://doi.org/10.1056/NEJMc2102017.
12. Madhi SA, Baillie V, Cutland CL, Voysey M, Koen AL, Fairlie L, Padayachee SD, Dheda K, Barnabas SL, Bhorat QE, Briner C, Kwatra G, Ahmed K, Aley P, Bhikha S, Bhiman JN, Bhorat AE, Du Plessis J, Esmail A, Groenewald M, Horne E, Hwa S-H, Jose A, Lambe T, Laubscher M, Malahleha M, Masenya M, Masilela M, McKenzie S, Molapo K, Moultrie A, Oelofse S, Patel F, Pillay S, Rhead S, Rodel H, Rossouw L, Taoushanis C, Tegally H, Thombrayil A, van Eck S, Wibmer CK, Durham NM, Kelly EJ, Villafana TL, Gilbert S, Pollard AJ, de Oliveira T, Moore PL, Sigal A, et al. 2021. Efficacy of the ChAdOx1 nCoV-19 Covid-19 Vaccine against the B.1.351 Variant. N Engl J Med 384:1885–1898. https://doi.org/10.1056/NEJMoa2102214.
13. Hoffmann M, Hofmann-Winkler H, Krüger N, Kempf A, Nehlmeier I, Graichen L, Sidarovich A, Moldenhauer A-S, Winkler MS, Schulz S, Jäck H-M, Stankov MV, Behrens GMN, Pöhlmann S. 5 May 2021. SARS-CoV-2 variant B.1.617 is resistant to Bamlanivimab and evades antibodies induced by infection and vaccination. bioRxiv https://doi.org/10.1101/2021.05.04.442663.
14. Garcia-Beltran WF, Lam EC, St Denis K, Nitido AD, Garcia ZH, Hauser BM, Feldman J, Pavlovic MN, Gregory DJ, Poznansky MC, Sigal A, Schmidt AG, Iafrate AJ, Naranbhai V, Balazs AB. 2021. Multiple SARS-CoV-2 variants escape neutralization by vaccine-induced humoral immunity. Cell 184:2372–2383.e9. https://doi.org/10.1016/j.cell.2021.03.013.
15. Hoffmann M, Arora P, Groß R, Seidel A, Hörnich BF, Hahn AS, Krüger N, Graichen L, Hofmann-Winkler H, Kempf A, Winkler MS, Schulz S, Jäck H-M, Jahrsdörfer B, Schrezenmeier H, Müller M, Kleger A, Münch J, Pöhlmann S. 2021. SARS-CoV-2 variants B.1.351 and P.1 escape from neutralizing antibodies. Cell 184:2384–2393.e12. https://doi.org/10.1016/j.cell.2021.03.036.
16. Wang P, Casner RG, Nair MS, Wang M, Yu J, Cerutti G, Liu L, Kwong PD, Huang Y, Shapiro L, Ho DD. 2021. Increased resistance of SARS-CoV-2 variant P.1 to antibody neutralization. Cell Host Microbe 29:747–751.e4. https://doi.org/10.1016/j.chom.2021.04.007.
17. Cameroni E, Bowen JE, Rosen LE, Saliba C, Zepeda SK, Culap K, Pinto D, VanBlargan LA, De Marco A, di Iulio J, Zatta F, Kaiser H, Noack J, Farhat N, Czudnochowski N, Havenar-Daughton C, Sprouse KR, Dillen JR, Powell AE, Chen A, Maher C, Yin L, Sun D, Soriaga L, Bassi J, Silacci-Fregni C, Gustafsson C, Franko NM, Logue J, Iqbal NT, Mazzitelli I, Geffner J, Grifantini R, Chu H, Gori A, Riva A, Giannini O, Ceschi A, Ferrari P, Cippà PE, Franzetti-Pellanda A, Garzoni C, Halfmann PJ, Kawaoka Y, Hebner C, Purcell LA, Piccoli L, Pizzuto MS, Walls AC, Diamond MS, et al. 23 December 2021. Broadly neutralizing antibodies overcome SARS-CoV-2 Omicron antigenic shift. Nature https://doi.org/10.1038/d41586-021-03825-4.
18. Cao Y, Wang J, Jian F, Xiao T, Song W, Yisimayi A, Huang W, Li Q, Wang P, An R, Wang J, Wang Y, Niu X, Yang S, Liang H, Sun H, Li T, Yu Y, Cui Q, Liu S, Yang X, Du S, Zhang Z, Hao X, Shao F, Jin R, Wang X, Xiao J, Wang Y, Xie XS. 23 December 2021. Omicron escapes the majority of existing SARS-CoV-2 neutralizing antibodies. Nature https://doi.org/10.1038/d41586-021-03796-6.
19. Liu L, Iketani S, Guo Y, Chan JF-W, Wang M, Liu L, Luo Y, Chu H, Huang Y, Nair MS, Yu J, Chik KK-H, Yuen TT-T, Yoon C, To KK-W, Chen H, Yin MT, Sobieszczyk ME, Huang Y, Wang HH, Sheng Z, Yuen K-Y, Ho DD. 23 December 2021. Striking antibody evasion manifested by the Omicron variant of SARS-CoV-2. Nature https://doi.org/10.1038/d41586-021-03826-3.
20. Carazo S, Talbot D, Boulianne N, Brisson M, Gilca R, Deceuninck G, Brousseau N, Drolet M, Ouakki M, Sauvageau C, Barkati S, Fortin E, Carignan A, De Wals P, Skowronski DM, De Serres G. 30 August 2021. Single-dose mRNA vaccine effectiveness against SARS-CoV-2 in healthcare

workers extending 16 weeks post-vaccination: a test-negative design from Quebec, Canada. Clin Infect Dis https://doi.org/10.1093/cid/ciab739.

21. Skowronski DM, Setayeshgar S, Zou M, Prystajecky N, Tyson JR, Galanis E, Naus M, Patrick DM, Sbihi H, El Adam S, Henry B, Hoang LMN, Sadarangani M, Jassem AN, Krajden M. 9 July 2021. Single-dose mRNA vaccine effectiveness against SARS-CoV-2, including Alpha and Gamma variants: a test-negative design in adults 70 years and older in British Columbia, Canada. Clin Infect Dis https://doi.org/10.1093/cid/ciab616.

22. US Food and Drug Administration. 2021. SARS-CoV-2 viral mutations: impact on COVID-19 tests. https://www.fda.gov/medical-devices/coronavirus-covid-19-and-medical-devices/sars-cov-2-viral-mutations-impact-covid-19-tests.

23. Wu K, Werner AP, Moliva JI, Koch M, Choi A, Stewart-Jones GBE, Bennett H, Boyoglu-Barnum S, Shi W, Graham BS, Carfi A, Corbett KS, Seder RA, Edwards DK. 25 January 2021. mRNA-1273 vaccine induces neutralizing antibodies against spike mutants from global SARS-CoV-2 variants. bioRxiv https://doi.org/10.1101/2021.01.25.427948.

24. Pouwels KB, Pritchard E, Matthews PC, Stoesser N, Eyre DW, Vihta K-D, House T, Hay J, Bell JI, Newton JN, Farrar J, Crook D, Cook D, Rourke E, Studley R, Peto T, Diamond I, Walker AS, COVID-19 Infection Survey Team. 24 August 2021. Impact of Delta on viral burden and vaccine effectiveness against new SARS-CoV-2 infections in the UK. https://doi.org/10.1101/2021.08.18.21262237.

25. Korber B, Fischer WM, Gnanakaran S, Yoon H, Theiler J, Abfalterer W, Hengartner N, Giorgi EE, Bhattacharya T, Foley B, Hastie KM, Parker MD, Partridge DG, Evans CM, Freeman TM, de Silva TI, Sheffield C-GG, McDanal C, Perez LG, Tang H, Moon-Walker A, Whelan SP, LaBranche CC, Saphire EO, Montefiori DC, Sheffield COVID-19 Genomics Group. 2020. Tracking changes in SARS-CoV-2 spike: evidence that D614G increases infectivity of the COVID-19 virus. Cell 182:812–827.e19. https://doi.org/10.1016/j.cell.2020.06.043.

26. Harvey WT, Carabelli AM, Jackson B, Gupta RK, Thomson EC, Harrison EM, Ludden C, Reeve R, Rambaut A, Consortium C-GU, Peacock SJ, Robertson DL, COVID-19 Genomics UK (COG-UK) Consortium. 2021. SARS-CoV-2 variants, spike mutations and immune escape. Nat Rev Microbiol 19: 409–424. https://doi.org/10.1038/s41579-021-00573-0.

27. Wise J. 2021. Covid-19: the E484K mutation and the risks it poses. BMJ 372:n359. https://doi.org/10.1136/bmj.n359.

28. Gong SY, Chatterjee D, Richard J, Prevost J, Tauzin A, Gasser R, Bo Y, Vezina D, Goyette G, Gendron-Lepage G, Medjahed H, Roger M, Cote M, Finzi A. 2021. Contribution of single mutations to selected SARS-CoV-2 emerging variants spike antigenicity. Virology 563:134–145. https://doi.org/10.1016/j.virol.2021.09.001.

29. Hoffmann M, Kleine-Weber H, Schroeder S, Kruger N, Herrler T, Erichsen S, Schiergens TS, Herrler G, Wu NH, Nitsche A, Muller MA, Drosten C, Pohlmann S. 2020. SARS-CoV-2 cell entry depends on ACE2 and TMPRSS2 and is blocked by a clinically proven protease inhibitor. Cell 181:271–280. https://doi.org/10.1016/j.cell.2020.02.052.

30. Hoffmann M, Kleine-Weber H, Pohlmann S. 2020. A multibasic cleavage site in the spike protein of SARS-CoV-2 is essential for infection of human lung cells. Mol Cell 78:779–784. https://doi.org/10.1016/j.molcel.2020.04.022.

31. Wang Q, Zhang Y, Wu L, Niu S, Song C, Zhang Z, Lu G, Qiao C, Hu Y, Yuen KY, Wang Q, Zhou H, Yan J, Qi J. 2020. Structural and functional basis of SARS-CoV-2 entry by using human ACE2. Cell 181:894–904. https://doi.org/10.1016/j.cell.2020.03.045.

32. Walls AC, Park YJ, Tortorici MA, Wall A, McGuire AT, Veesler D. 2020. Structure, function, and antigenicity of the SARS-CoV-2 spike glycoprotein. Cell 181:281–292. https://doi.org/10.1016/j.cell.2020.02.058.

33. Cai Y, Zhang J, Xiao T, Peng H, Sterling SM, Walsh RM, Jr, Rawson S, Rits-Volloch S, Chen B. 2020. Distinct conformational states of SARS-CoV-2 spike protein. Science 369:1586–1592. https://doi.org/10.1126/science.abd4251.

34. Ke Z, Oton J, Qu K, Cortese M, Zila V, McKeane L, Nakane T, Zivanov J, Neufeldt CJ, Cerikan B, Lu JM, Peukes J, Xiong X, Krausslich HG, Scheres SHW, Bartenschlager R, Briggs JAG. 2020. Structures and distributions of SARS-CoV-2 spike proteins on intact virions. Nature 588:498–502. https://doi.org/10.1038/s41586-020-2665-2.

35. Shang J, Wan Y, Luo C, Ye G, Geng Q, Auerbach A, Li F. 2020. Cell entry mechanisms of SARS-CoV-2. Proc Natl Acad Sci U S A 117:11727–11734. https://doi.org/10.1073/pnas.2003138117.

36. Belouzard S, Millet JK, Licitra BN, Whittaker GR. 2012. Mechanisms of coronavirus cell entry mediated by the viral spike protein. Viruses 4: 1011–1033. https://doi.org/10.3390/v4061011.

37. Lu M. 2021. Single-molecule FRET imaging of virus spike-host interactions. Viruses 13:332. https://doi.org/10.3390/v13020332.

38. Benton DJ, Wrobel AG, Xu P, Roustan C, Martin SR, Rosenthal PB, Skehel JJ, Gamblin SJ. 2020. Receptor binding and priming of the spike protein of SARS-CoV-2 for membrane fusion. Nature 588:327–330. https://doi.org/10.1038/s41586-020-2772-0.

39. Henderson R, Edwards RJ, Mansouri K, Janowska K, Stalls V, Gobeil SMC, Kopp M, Li D, Parks R, Hsu AL, Borgnia MJ, Haynes BF, Acharya P. 2020. Controlling the SARS-CoV-2 spike glycoprotein conformation. Nat Struct Mol Biol 27:925–933. https://doi.org/10.1038/s41594-020-0479-4.

40. Hsieh CL, Goldsmith JA, Schaub JM, DiVenere AM, Kuo HC, Javanmardi K, Le KC, Wrapp D, Lee AG, Liu Y, Chou CW, Byrne PO, Hjorth CK, Johnson NV, Ludes-Meyers J, Nguyen AW, Park J, Wang N, Amengor D, Lavinder JJ, Ippolito GC, Maynard JA, Finkelstein IJ, McLellan JS. 2020. Structure-based design of prefusion-stabilized SARS-CoV-2 spikes. Science 369:1501–1505. https://doi.org/10.1126/science.abd0826.

41. Lan J, Ge J, Yu J, Shan S, Zhou H, Fan S, Zhang Q, Shi X, Wang Q, Zhang L, Wang X. 2020. Structure of the SARS-CoV-2 spike receptor-binding domain bound to the ACE2 receptor. Nature 581:215–220. https://doi.org/10.1038/s41586-020-2180-5.

42. Liu L, Wang P, Nair MS, Yu J, Rapp M, Wang Q, Luo Y, Chan JF, Sahi V, Figueroa A, Guo XV, Cerutti G, Bimela J, Gorman J, Zhou T, Chen Z, Yuen KY, Kwong PD, Sodroski JG, Yin MT, Sheng Z, Huang Y, Shapiro L, Ho DD. 2020. Potent neutralizing antibodies against multiple epitopes on SARS-CoV-2 spike. Nature 584:450–456. https://doi.org/10.1038/s41586-020-2571-7.

43. McCallum M, Walls AC, Bowen JE, Corti D, Veesler D. 2020. Structure-guided covalent stabilization of coronavirus spike glycoprotein trimers in the closed conformation. Nat Struct Mol Biol 27:942–949. https://doi.org/10.1038/s41594-020-0483-8.

44. Shang J, Ye G, Shi K, Wan Y, Luo C, Aihara H, Geng Q, Auerbach A, Li F. 2020. Structural basis of receptor recognition by SARS-CoV-2. Nature 581: 221–224. https://doi.org/10.1038/s41586-020-2179-y.

45. Wrapp D, Wang N, Corbett KS, Goldsmith JA, Hsieh CL, Abiona O, Graham BS, McLellan JS. 2020. Cryo-EM structure of the 2019-nCoV spike in the prefusion conformation. Science 367:1260–1263. https://doi.org/10.1126/science.abb2507.

46. Yao H, Song Y, Chen Y, Wu N, Xu J, Sun C, Zhang J, Weng T, Zhang Z, Wu Z, Cheng L, Shi D, Lu X, Lei J, Crispin M, Shi Y, Li L, Li S. 2020. Molecular architecture of the SARS-CoV-2 virus. Cell 183:730–738.e13. https://doi.org/10.1016/j.cell.2020.09.018.

47. Wu A, Wang L, Zhou HY, Ji CY, Xia SZ, Cao Y, Meng J, Ding X, Gold S, Jiang T, Cheng G. 2021. One year of SARS-CoV-2 evolution. Cell Host Microbe 29:503–507. https://doi.org/10.1016/j.chom.2021.02.017.

48. Dong E, Du H, Gardner L. 2020. An interactive web-based dashboard to track COVID-19 in real time. Lancet Infect Dis 20:533–534. https://doi.org/10.1016/S1473-3099(20)30120-1.

49. Du Plessis L, McCrone JT, Zarebski AE, Hill V, Ruis C, Gutierrez B, Raghwani J, Ashworth J, Colquhoun R, Connor TR, Faria NR, Jackson B, Loman NJ, O'Toole A, Nicholls SM, Parag KV, Scher E, Vasylyeva TI, Volz EM, Watts A, Bogoch II, Khan K, Consortium C-GU, Aanensen DM, Kraemer MUG, Rambaut A, Pybus OG, COVID-19 Genomics UK (COG-UK) Consortium. 2021. Establishment and lineage dynamics of the SARS-CoV-2 epidemic in the UK. Science 371:708–712. https://doi.org/10.1126/science.abf2946.

50. Msomi N, Mlisana K, de Oliveira T, Network for Genomic Surveillance in South Africa writing group. 2020. A genomics network established to respond rapidly to public health threats in South Africa. Lancet Microbe 1:e229–e230. https://doi.org/10.1016/S2666-5247(20)30116-6.

51. Zhang J, Cai Y, Xiao T, Lu J, Peng H, Sterling SM, Walsh RM, Jr, Rits-Volloch S, Zhu H, Woosley AN, Yang W, Sliz P, Chen B. 2021. Structural impact on SARS-CoV-2 spike protein by D614G substitution. Science 372:525–530. https://doi.org/10.1126/science.abf2303.

52. Benton DJ, Wrobel AG, Roustan C, Borg A, Xu P, Martin SR, Rosenthal PB, Skehel JJ, Gamblin SJ. 2021. The effect of the D614G substitution on the structure of the spike glycoprotein of SARS-CoV-2. Proc Natl Acad Sci U S A 118:e2022586118. https://doi.org/10.1073/pnas.2022586118.

53. Gobeil SM-C, Janowska K, McDowell S, Mansouri K, Parks R, Manne K, Stalls V, Kopp MF, Henderson R, Edwards RJ, Haynes BF, Acharya P. 2021. D614G mutation alters SARS-CoV-2 spike conformation and enhances protease cleavage at the S1/S2 junction. Cell Rep 34:108630. https://doi.org/10.1016/j.celrep.2020.108630.

54. Yurkovetskiy L, Wang X, Pascal KE, Tomkins-Tinch C, Nyalile TP, Wang Y, Baum A, Diehl WE, Dauphin A, Carbone C, Veinotte K, Egri SB, Schaffner SF, Lemieux JE, Munro JB, Rafique A, Barve A, Sabeti PC, Kyratsous CA, Dudkina NV, Shen K, Luban J. 2020. Structural and functional analysis of the D614G SARS-CoV-2 spike protein variant. Cell 183:739–751.e8. https://doi.org/10.1016/j.cell.2020.09.032.

55. Gobeil SM, Janowska K, McDowell S, Mansouri K, Parks R, Stalls V, Kopp MF, Manne K, Li D, Wiehe K, Saunders KO, Edwards RJ, Korber B, Haynes BF, Henderson R, Acharya P. 2021. Effect of natural mutations of SARS-CoV-2 on spike structure, conformation, and antigenicity. Science 373: eabi6226. https://doi.org/10.1126/science.abi6226.

56. Cai Y, Zhang J, Xiao T, Lavine CL, Rawson S, Peng H, Zhu H, Anand K, Tong P, Gautam A, Lu S, Sterling SM, Walsh RM, Jr, Rits-Volloch S, Lu J, Wesemann DR, Yang W, Seaman MS, Chen B. 2021. Structural basis for enhanced infectivity and immune evasion of SARS-CoV-2 variants. Science 373:642–648. https://doi.org/10.1126/science.abi9745.

57. Li W, Chen Y, Prévost J, Ullah I, Lu M, Gong SY, Tauzin A, Gasser R, Vézina D, Anand SP, Goyette G, Chaterjee D, Ding S, Tolbert WD, Grunst MW, Bo Y, Zhang S, Richard J, Zhou F, Huang RK, Esser L, Zeher A, Côté M, Kumar P, Sodroski J, Xia D, Uchil PD, Pazgier M, Finzi A, Mothes W. 2022. Structural basis and mode of action for two broadly neutralizing antibodies against SARS-CoV-2 emerging variants of concern. Cell Rep 38:110210. https://doi.org/10.1016/j.celrep.2021.110210.

58. Lu M, Uchil PD, Li W, Zheng D, Terry DS, Gorman J, Shi W, Zhang B, Zhou T, Ding S, Gasser R, Prevost J, Beaudoin-Bussieres G, Anand SP, Laumaea A, Grover JR, Liu L, Ho DD, Mascola JR, Finzi A, Kwong PD, Blanchard SC, Mothes W. 2020. Real-time conformational dynamics of SARS-CoV-2 spikes on virus particles. Cell Host Microbe 28:880–891.e8. https://doi.org/10.1016/j.chom.2020.11.001.

59. Sztain T, Ahn SH, Bogetti AT, Casalino L, Goldsmith JA, Seitz E, McCool RS, Kearns FL, Acosta-Reyes F, Maji S, Mashayekhi G, McCammon JA, Ourmazd A, Frank J, McLellan JS, Chong LT, Amaro RE. 2021. A glycan gate controls opening of the SARS-CoV-2 spike protein. Nat Chem 13:963–968. https://doi.org/10.1038/s41557-021-00758-3.

60. Lu M, Ma X, Castillo-Menendez LR, Gorman J, Alsahafi N, Ermel U, Terry DS, Chambers M, Peng D, Zhang B, Zhou T, Reichard N, Wang K, Grover JR, Carman BP, Gardner MR, Nikic-Spiegel I, Sugawara A, Arthos J, Lemke EA, Smith AB, III, Farzan M, Abrams C, Munro JB, McDermott AB, Finzi A, Kwong PD, Blanchard SC, Sodroski JG, Mothes W. 2019. Associating HIV-1 envelope glycoprotein structures with states on the virus observed by smFRET. Nature 568:415–419. https://doi.org/10.1038/s41586-019-1101-y.

61. Munro JB, Gorman J, Ma X, Zhou Z, Arthos J, Burton DR, Koff WC, Courter JR, Smith AB, III, Kwong PD, Blanchard SC, Mothes W. 2014. Conformational dynamics of single HIV-1 envelope trimers on the surface of native virions. Science 346:759–763. https://doi.org/10.1126/science.1254426.

62. Lin CW, Ting AY. 2006. Transglutaminase-catalyzed site-specific conjugation of small-molecule probes to proteins in vitro and on the surface of living cells. J Am Chem Soc 128:4542–4543. https://doi.org/10.1021/ja0604111.

63. Yin J, Lin AJ, Golan DE, Walsh CT. 2006. Site-specific protein labeling by Sfp phosphopantetheinyl transferase. Nat Protoc 1:280–285. https://doi.org/10.1038/nprot.2006.43.

64. Ozono S, Zhang Y, Ode H, Sano K, Tan TS, Imai K, Miyoshi K, Kishigami S, Ueno T, Iwatani Y, Suzuki T, Tokunaga K. 2021. SARS-CoV-2 D614G spike mutation increases entry efficiency with enhanced ACE2-binding affinity. Nat Commun 12:848. https://doi.org/10.1038/s41467-021-21118-2.

65. Khan A, Zia T, Suleman M, Khan T, Ali SS, Abbasi AA, Mohammad A, Wei DQ. 2021. Higher infectivity of the SARS-CoV-2 new variants is associated with K417N/T, E484K, and N501Y mutants: an insight from structural data. J Cell Physiol 236:7045–7057. https://doi.org/10.1002/jcp.30367.

66. McKinney SA, Joo C, Ha T. 2006. Analysis of single-molecule FRET trajectories using hidden Markov modeling. Biophys J 91:1941–1951. https://doi.org/10.1529/biophysj.106.082487.

67. Prevost J, Finzi A. 2021. The great escape? SARS-CoV-2 variants evading neutralizing responses. Cell Host Microbe 29:322–324. https://doi.org/10.1016/j.chom.2021.02.010.

68. Prevost J, Richard J, Gasser R, Ding S, Fage C, Anand SP, Adam D, Gupta Vergara N, Tauzin A, Benlarbi M, Gong SY, Goyette G, Prive A, Moreira S, Charest H, Roger M, Mothes W, Pazgier M, Brochiero E, Boivin G, Abrams CF, Schon A, Finzi A. 2021. Impact of temperature on the affinity of SARS-CoV-2 spike glycoprotein for host ACE2. J Biol Chem 297:101151. https://doi.org/10.1016/j.jbc.2021.101151.

69. Ullah I, Prevost J, Ladinsky MS, Stone H, Lu M, Anand SP, Beaudoin-Bussieres G, Symmes K, Benlarbi M, Ding S, Gasser R, Fink C, Chen Y, Tauzin A, Goyette G, Bourassa C, Medjahed H, Mack M, Chung K, Wilen CB, Dekaban GA, Dikeakos JD, Bruce EA, Kaufmann DE, Stamatatos L, McGuire AT, Richard J, Pazgier M, Bjorkman PJ, Mothes W, Finzi A, Kumar P, Uchil PD. 2021. Live imaging of SARS-CoV-2 infection in mice reveals neutralizing antibodies require Fc function for optimal efficacy. Immunity 54:2143–2158.e15. https://doi.org/10.1016/j.immuni.2021.08.015.

70. Plante JA, Liu Y, Liu J, Xia H, Johnson BA, Lokugamage KG, Zhang X, Muruato AE, Zou J, Fontes-Garfias CR, Mirchandani D, Scharton D, Bilello JP, Ku Z, An Z, Kalveram B, Freiberg AN, Menachery VD, Xie X, Plante KS, Weaver SC, Shi PY. 2021. Spike mutation D614G alters SARS-CoV-2 fitness. Nature 592:116–121. https://doi.org/10.1038/s41586-020-2895-3.

71. Zhou B, Thao TTN, Hoffmann D, Taddeo A, Ebert N, Labroussaa F, Pohlmann A, King J, Steiner S, Kelly JN, Portmann J, Halwe NJ, Ulrich L, Trueb BS, Fan X, Hoffmann B, Wang L, Thomann L, Lin X, Stalder H, Pozzi B, de Brot S, Jiang N, Cui D, Hossain J, Wilson MM, Keller MW, Stark TJ, Barnes JR, Dijkman R, Jores J, Benarafa C, Wentworth DE, Thiel V, Beer M. 2021. SARS-CoV-2 spike D614G change enhances replication and transmission. Nature 592:122–127. https://doi.org/10.1038/s41586-021-03361-1.

72. Wec AZ, Wrapp D, Herbert AS, Maurer DP, Haslwanter D, Sakharkar M, Jangra RK, Dieterle ME, Lilov A, Huang D, Tse LV, Johnson NV, Hsieh CL, Wang N, Nett JH, Champney E, Burnina I, Brown M, Lin S, Sinclair M, Johnson C, Pudi S, Bortz R, III, Wirchnianski AS, Laudermilch E, Florez C, Fels JM, O'Brien CM, Graham BS, Nemazee D, Burton DR, Baric RS, Voss JE, Chandran K, Dye JM, McLellan JS, Walker LM. 2020. Broad neutralization of SARS-related viruses by human monoclonal antibodies. Science 369: 731–736. https://doi.org/10.1126/science.abc7424.

73. Long Y, Song S, Luo F, Han X, Hu C, Wang Y, Li S, Wang W, Zhang H, Zhang H, Li T, Jin A. 2021. A non-RBM targeted RBD specific antibody neutralizes SARS-CoV-2 inducing S1 shedding. Biochem Biophys Res Commun 571:152–158. https://doi.org/10.1016/j.bbrc.2021.07.062.

74. Jangra S, Ye C, Rathnasinghe R, Stadlbauer D, Krammer F, Simon V, Martinez-Sobrido L, Garcia-Sastre A, Schotsaert M, Personalized Virology Initiative study group. 2021. SARS-CoV-2 spike E484K mutation reduces antibody neutralisation. Lancet Microbe 2:e283–e284. https://doi.org/10.1016/S2666-5247(21)00068-9.

75. Baum A, Fulton BO, Wloga E, Copin R, Pascal KE, Russo V, Giordano S, Lanza K, Negron N, Ni M, Wei Y, Atwal GS, Murphy AJ, Stahl N, Yancopoulos GD, Kyratsous CA. 2020. Antibody cocktail to SARS-CoV-2 spike protein prevents rapid mutational escape seen with individual antibodies. Science 369: 1014–1018. https://doi.org/10.1126/science.abd0831.

76. Weisblum Y, Schmidt F, Zhang F, DaSilva J, Poston D, Lorenzi JC, Muecksch F, Rutkowska M, Hoffmann HH, Michailidis E, Gaebler C, Agudelo M, Cho A, Wang Z, Gazumyan A, Cipolla M, Luchsinger L, Hillyer CD, Caskey M, Robbiani DF, Rice CM, Nussenzweig MC, Hatziioannou T, Bieniasz PD. 2020. Escape from neutralizing antibodies by SARS-CoV-2 spike protein variants. Elife 9:e61312. https://doi.org/10.7554/eLife.61312.

77. Prevost J, Gasser R, Beaudoin-Bussieres G, Richard J, Duerr R, Laumaea A, Anand SP, Goyette G, Benlarbi M, Ding S, Medjahed H, Lewin A, Perreault J, Tremblay T, Gendron-Lepage G, Gauthier N, Carrier M, Marcoux D, Piche A, Lavoie M, Benoit A, Loungnarath V, Brochu G, Haddad E, Stacey HD, Miller MS, Desforges M, Talbot PJ, Maule GTG, Cote M, Therrien C, Serhir B, Bazin R, Roger M, Finzi A. 2020. Cross-sectional evaluation of humoral responses against SARS-CoV-2 spike. Cell Rep Med 1:100126. https://doi.org/10.1016/j.xcrm.2020.100126.

78. Jin J, Sherer NM, Heidecker G, Derse D, Mothes W. 2009. Assembly of the murine leukemia virus is directed towards sites of cell-cell contact. PLoS Biol 7:e1000163. https://doi.org/10.1371/journal.pbio.1000163.

79. Zhong P, Agosto LM, Ilinskaya A, Dorjbal B, Truong R, Derse D, Uchil PD, Heidecker G, Mothes W. 2013. Cell-to-cell transmission can overcome multiple donor and target cell barriers imposed on cell-free HIV. PLoS One 8:e53138. https://doi.org/10.1371/journal.pone.0053138.

80. Zhou T, Teng IT, Olia AS, Cerutti G, Gorman J, Nazzari A, Shi W, Tsybovsky Y, Wang L, Wang S, Zhang B, Zhang Y, Katsamba PS, Petrova Y, Banach BB, Fahad AS, Liu L, Lopez Acevedo SN, Madan B, Oliveira de Souza M, Pan X, Wang P, Wolfe JR, Yin M, Ho DD, Phung E, DiPiazza A, Chang LA, Abiona OM, Corbett KS, DeKosky BJ, Graham BS, Mascola JR, Misasi J, Ruckwardt T, Sullivan NJ, Shapiro L, Kwong PD. 2020. Structure-based design with tag-based purification and in-process biotinylation enable streamlined development of SARS-CoV-2 spike molecular probes. Cell Rep 33:108322. https://doi.org/10.1016/j.celrep.2020.108322.

81. Ma X, Lu M, Gorman J, Terry DS, Hong X, Zhou Z, Zhao H, Altman RB, Arthos J, Blanchard SC, Kwong PD, Munro JB, Mothes W. 2018. HIV-1 Env trimer opens through an asymmetric intermediate in which individual protomers adopt distinct conformations. Elife 7:e34271. https://doi.org/10.7554/eLife.34271.

82. Pati AK, El Bakouri O, Jockusch S, Zhou Z, Altman RB, Fitzgerald GA, Asher WB, Terry DS, Borgia A, Holsey MD, Batchelder JE, Abeywickrama C, Huddle B, Rufa D, Javitch JA, Ottosson H, Blanchard SC. 2020. Tuning

the Baird aromatic triplet-state energy of cyclooctatetraene to maximize the self-healing mechanism in organic fluorophores. Proc Natl Acad Sci U S A 117:24305–24315. https://doi.org/10.1073/pnas .2006517117.

83. Aitken CE, Marshall RA, Puglisi JD. 2008. An oxygen scavenging system for improvement of dye stability in single-molecule fluorescence experiments. Biophys J 94:1826–1835. https://doi.org/10.1529/biophysj .107.117689.

84. Juette MF, Terry DS, Wasserman MR, Altman RB, Zhou Z, Zhao H, Blanchard SC. 2016. Single-molecule imaging of non-equilibrium molecular ensembles on the millisecond timescale. Nat Methods 13:341–344. https://doi.org/10 .1038/nmeth.3769.